GCAGS JOURNAL
A Publication of the Gulf Coast Association of Geological Societies
www.gcags.org

Effects of Salinization Pathways upon Morphogenic and Geochemical Features of Coastal-Margin Vertisols, Aransas National Wildlife Refuge, Aransas County, Texas

Sarah J. Kogler and Steven G. Driese

Department of Geosciences, Baylor University, One Bear Place #97354, Waco, Texas 76798–7354, U.S.A.

ABSTRACT

Coastal regions are predicted to experience changes in hydrology in response to climate-induced increases in sea-surface temperatures, sea-level rise, and shifts in weather patterns. These changes will likely alter pathways that marine salts enter coastal soils. This study aims to identify and quantify physical and geochemical changes in salt-affected vertisols and vertic intergrades forming on the Texas Gulf Coast. The characteristic morphogenic features of vertisols are formed as expandable clays experience seasonal fluctuations in moisture content within the profile, and smectite-group clays are more salt-sensitive than other clay types. This, coupled with their prevalence in low-lying coastal regions, makes the vertisol soil order useful for exploring how active pedogenic processes may respond to future climate scenarios.

Soils were described and sampled along two transects in the Tatton Unit of Aransas National Wildlife Refuge from the coast of St. Charles Bay inland, including environments ranging from saline coastal prairie to saline-to-brackish tidal flats and tidal marshes. Macro- and micromorphological pedogenic features and geochemical patterns of major cations observed along each transect allowed for the interpretation of the relative influence of salinization pathways at the reserve based on distance from the coast and landscape position. Evidence of salinization due to underlying brackish groundwater was observed along both transects. In contrast, salinization due to surface inputs from marine sediment, tidal influence, and storm surge was more prevalent within the floodplain and at most coastal upland sites. Along both transects, slickensides and desiccation cracks appeared to be limited to the most well-drained upland sites, suggesting that a combination of increased saturation and salinization may be suppressing the formation of macroscopic vertic features.

INTRODUCTION

Salinization occurs when water-soluble salts accumulate in the soil body to concentrations that impact agricultural production, environmental health, and economic interests (Table 1) (Rengasamy, 2006). The global extent of salt-affected soils (SAS) varies. Food and Agriculture Organization of the United Nations (FAO) global SAS mapping initiatives estimated that 434 Mha of topsoil and 833 Mha of subsoil are salt-affected (FAO, 2021), whereas estimates from the Harmonized World Soil Database found approximately 1128 Mha of SAS, (Wicke et al., 2011). Soil degradation from salts is expected to increase in future climate-change scenarios as existing salt-affected areas expand and new areas are created (Schofield and Kirkby, 2003). Salinization processes include groundwater-associated salinization (GAS), non–GAS, and anthropogenic salinization (Table 2) (Rengasamy, 2006). GAS occurs in soils with restricted permeability, most prevalently in topographic microlows, on floodplains, low terraces, or foot-slope positions (Junior et al., 2019). Salts accumulate in shallow or perched groundwater (GW) due to reduced leaching potential and precipitate in the rooting zone as GW is drawn upwards by evapotranspiration (ET), which may result in the formation of a restrictive horizon (Rengasamy, 2006). In areas with shallow GW and strong surface-GW interchange, salts from saline GW may enter the soil by surface streamflow (Daliakopoulos, 2016). Wet deposition through precipitation, dry deposition of aeolian materials, and physical or chemical weathering of primary minerals all contribute to primary non–GAS (Rengasamy, 2006; Hassani et al., 2021). Salts can be introduced through poor-quality, often recycled irrigation water, especially in poorly drained soils with high ET (Rengasamy, 2006). Poor land management in coastal regions may cause local rises in the water table or surface or subsurface seawater intrusion into coastal aquifers from sea-level rise or over-exploitation of potable aquifers (Daliakopoulos, 2016).

Manuscript received May 22, 2023; revised manuscript received August 21, 2023; manuscript accepted August 21, 2023.

GCAGS Journal, v. 12 (2023), p. 76–96.
https://doi.org/10.62371/BAVM1215

Table 1. Classification of salt-affected soils (Richards, 1954).

Classification	Electrical Conductivity (dS/m)	Sodium Adsorption Ratio	Exchangeable Sodium Percentage
Saline	>4.0	<13	<15
Sodic	<4.0	>13	>15
Saline-Sodic	>4.0	>13	>15

Table 2. Primary and secondary sources of salinity and environmental impacts of soil salinization.

Ion	Sources	Environmental Impact	References
Na^+	Parent rock weathering, SI, saline-brackish GW, wet and dry deposition of marine-derived salts, poor quality irrigation water, road salt	Plant and microbial osmotic effects and ionic toxicity; reduces nutrient cycling; clay dispersion, loss of soil structure, weakened hydraulic properties, susceptibility to erosion, runoff, and crusting; salinization of freshwater bodies, increased turbidity	Abrol et al. (1988); Qadir and Schubert (2002); Yan et al. (2015); Xie et al. (2022)
Ca^{2+}	Weathering of carbonate PM; weathering of gypsum, calcite, hornblende, plagioclase; aeolian deposition; pedogenic processes; marine surface inputs, SI; wet/dry deposition of marine-derived salts; fertilizer	Limited detrimental effects; improves soil structure relative to Mg/Na; indirect toxicity by limiting absorption of Mg, K, P, Cu, Zn, Fe, B; increases silt size fraction; increases soil pH; forms restrictive layers or crusts in arid regions	White and Broadley (2003); Taalab et al., 2019)
Mg^{2+}	Parent rock weathering (silicate and carbonate bedrock), poor quality irrigation water, municipal and industrial wastewater	Reduced soil structure, reduced hydraulic conductivity, yield reduction in sensitive species	Qadir et al. (2018)
Cl^-	Parent rock weathering (mafic bedrocks and evaporites), SI, saline-brackish GW, wet/dry deposition of marine-derived salts, poor quality irrigation water, fertilizer, road salt, chlorinated pollutants	Plant and microbial osmotic effects and ionic toxicity	Svensson et al. (2021); Geilfus (2019)
SO_4^{2-}	Dissolution/oxidation of sulfate minerals, SI, storm deposits, OM decomposition, fertilizer, wet/dry deposition of marine or industrially derived particulates	Interferes with uptake of Ca, Mg, P; osmotic stress; promotes Na toxicity; forms of acid sulfate soils; reduction to H_2S (buffered by iron and pyrite formation)	Reich et al. (2017); Sawyer et al. (2016); Tully et al. (2019a)
P (inorg.)	SI, parent rock weathering, legacy fertilizer	Eutrophication of coastal waterways, interferes with Zn and Fe absorption in plants	Tully et al. (2019b); Weissman and Tully (2020)

Changes in hydrology associated with sea level rise (SLR) are expected to alter salinization pathways for coastal soils. Climate models project a higher probability of precipitation globally and changes in seasonal precipitation intensity, with a transition towards higher-intensity events on land (Feng et al., 2019). Sea-surface temperature (SST) increases, and SLR are projected to alter the intensity of storm precipitation, storm surge, and the pattern of storm surge (Mousavi et al., 2011). TDS and salinity signatures from storm surge can persist for eight years before flushing from surficial aquifers into surrounding waterbodies by precipitation alone (Xiao et al., 2019). Areas not at risk of direct flooding can still be subject to inundation as water levels in unconfined aquifers rise (Rotzoll and Fletcher, 2012). Saltwater intrusion (SI) can change the overall water chemistry, density, and distribution of salts within coastal aquifers; controlled by the magnitude of fresh GW discharge, which is influenced by precipitation, local aquifer composition, and hydraulic conductivity, and the GW recharge rate, which is influenced by local land cover, land use, and permeability (Ketabchi et al., 2016).

Globally, the primary indicators for SAS are low relief and high two-way annual moisture flux, which favor salt accumulation that is localized or has a catenary relationship, with a third indicator being local flow deficits in large catchments leading to salt accumulation in floodplains and adjacent irrigated areas (Schofield and Kirkby, 2003). In coastal regions, salinization factors often act in contrasting directions, and the extent and consequences of salinization of coastal soils are still difficult to predict globally (Mazhar et al., 2022). Coastal salinization is driven by salinity (chlorides and sulfates of Na^+, Ca^{2+}, and Mg^{2+}, rather than alkalinity (Na and other carbonates) (Xie et al., 2022). Seawater moving into terrestrial systems is recognizable because it has 400 times more salts than freshwater; with Ca^{2+}, Mg^{2+}, Na^+, K^+, and SO_4^{2-}, comprising 44% of total marine salts (Tully et al., 2019a). Modeling coastal salinization requires precise estimates of GW extraction from unconfined coastal aquifers and salinity changes within the aquifers to account for SI and GAS (Hassani et al., 2021). However, combining spatiotemporal salinity data with hydrological conductivity may allow for local modeling of surface soil salinity and exploring the effects of SI on coastal salt marsh systems, especially in naturally reserved regions (Sui et al., 2022).

Vertisols and vertic intergrades can be used to interpret the relative importance of salinization pathways along the Texas Gulf Coast and to predict how soils may respond as salinization pathways change in future climate scenarios. These pathways can be broadly grouped into responses to (A) increased direct marine and tidal inundation due to SLR, (B) projected drought due to increased evaporation as land and SST rise, (C) changes in rainfall with a transition to extreme precipitation events, and (D) increased anthropogenic demand. Vertisols were selected because they are classified as prone to salinization in the world reference base for soil resources (Daliakopoulos et al., 2016). We posited that coastal vertisols will exhibit changes in (1) observable macro and micromorphological features and (2) the distribution of major seawater cations and redox-sensitive elements with

depth in the profile as the dominant salinization pathway transitions from surface to groundwater with distance from the coast.

GEOLOGIC SETTING

The Aransas National Wildlife Refuge (ANWR) is a 46,400 ha preserve that was established in 1937 as a refuge and breeding ground for migratory birds and other wildlife in the Texas Coastal Bend in Aransas and Refugio counties (USFWS, 2010) (Fig. 1A). The Tatton Management Unit was added to the reserve in 1967 to preserve a remnant of low upland (dark soil) coastal prairie and associated wildlife and contains 3063 ha of low upland coastal prairie, coastal marshland, tidal shore grassland, and tidal flats (USFWS, 2010). Spring tides and wind forcing result in irregular inundation of salt marshes at ANWR, leading to a narrow fringe dominated by *Spartina alterniflora* L. that borders a mixed high-marsh community before grading into an upland transition zone dominated by *Spartina spartinae*, grasses, and sedges (Butzler and Davis, 2006).

The Tatton Unit is made up of clayey to silty, clayey, and fine-grained sandy Pleistocene deltaic deposits of the Beaumont Formation (Barnes, 1987) (Fig. 1B) that are overprinted by modern marsh tidal-flat systems (Tremblay et al., 2008). The high clay content and low relief favored the formation of nearly 4 Mha of vertisols on the Beaumont Formation along the Texas Coastal Plain (Coulombe et al., 1996). The Tatton Unit's soil is mapped as Aransas clay, Narta loam, Victine clay loam, and other fine-grained soils with saline, sodic, and vertic properties (SSS, 2023) (Table 3). The regional depositional history shows a shifting coastline; the underlying Lissie Formation includes bay fill/lagoon depositional facies, and the Goliad Formation includes bay fill/lagoon and shore zone facies (Young et al., 2010).

The Beaumont Clay is hydrologically connected to the underlying Goliad Sand and Lissie Formation, together forming the Gulf Coast aquifer (Shafer, 1970). The Tatton Unit is located within the Chicot hydrologic unit of the Gulf Coast aquifer (Baker, 1979). This unit is mainly slightly to moderately saline, and TDS concentrations from geophysical logs indicate that less than 20% of the total aquifer thickness is fresh water (Young et al., 2010). At the aquifer scale, over 83% of the variance of geochemical characteristics in the Chicot hydrologic unit can be explained by indices of ionic strength, alkalinity, recharge, and non-carbonate hardness, with surface–GW interactions at wells near rivers and streams having a greater influence than upland wells (Uddameri et al., 2014). Combined geochemical, isotopic, and flow-system information approaches suggest that although precipitation enriched with marine aerosols is the main source of GW salinity in the Gulf Coast Aquifer System (Chowdhury et al., 2018), SI may be locally significant. Wells within the Tatton Unit were labeled unfavorable for fresh groundwater development due to excess Cl- and the potential for vertical and horizontal SI (Shafer, 1970). Elevated K^+ and Br^-/Cl^- ratios indicate SI within portions of the Gulf Coast aquifer, including Aransas County (Chowdhury et al., 2006).

The Tatton Unit is located northwest of St. Charles Bay, a 33.9 km^2 secondary bay in the Mission-Aransas Estuary National Estuarine Research Reserve (NERR) (UT–MSI, 2015). Sediments within St. Charles Bay are primarily sands to silty sands (UT–MSI, 2015). Shallow water depths (less than 1 m) and low connectivity with marine waters cause conditions in this bay to be driven by freshwater influx, with high flows decreasing salinity and drought creating hypersaline conditions (Orlando et al., 1993). In drought years, high temperatures and low freshwater recharge can lead to temperatures within the bays high enough to drive out dissolved oxygen, resulting in fish kills (USFWS, 2010). St. Charles Bay is fed by Twin Creek, Salt Creek, and Cavasso Creek, which are tidally influenced, low-gradient sluggish streams (Shafer, 1970). It is classified as microtidal, with tides averaging 0.3–0.6 m (USFWS, 2010). Larger rivers in the Mission-Aransas NERR are low flow under normal conditions but deliver pulses of freshwater, nutrients, and organic matter during storm events (Mooney and McClelland, 2012). In 2007, salinity in Copano Bay decreased from 12 to 2‰ due to frequent storm events, increasing to 30‰ by December 2008 (Mooney and McClelland, 2012).

The climate at ANWR is maritime, humid, and subtropical, and soil climates are udic and hyperthermic (SSS, 1999; USFWS, 2010). Temperatures are moderated by the Gulf of Mexico, with coastal breezes reducing the summer temperatures to an average of 29.9°C. In contrast, the heat stored within the Gulf of Mexico increases mean winter temperatures to 12.8°C (USFWS, 2010). Summer winds are predominantly southeasterly off the Gulf of Mexico, while in the winter, high-pressure systems from Canada and the Pacific bring northerly winds that cause rapid temperature drops and low tides within the bays as water is forced eastward into the Gulf of Mexico (USACoE, 1995). ANWR's mean annual precipitation (MAP) is about 914-965 mm, with peaks in spring and early fall and typically dry summers punctuated by storm events (USACoE, 1995). Hurricanes and tropical storms result in intermittent standing water, but in normal rainfall and drought years, standing water is absent in most reserve (USFWS, 2010).

Ecosystems along the Texas Gulf Coast are well adapted to storm events, despite potential hazards associated with widespread coastal flooding, extreme rainfall, and associated winds (Pathak and Fuller, 2021). The average return frequency for hurricanes is about 1 in 2.5 yr along the Texas coast and 1 in 10 yr for any particular location (USACoE, 1995). Before Hurricane Harvey in 2017, the last major hurricane to land on the middle Texas Coast was Hurricane Celia in 1970 (NWS, 2017). Hurricane Harvey made landfall east of Rockport, Texas, and in Copano Bay as a Category 4 storm, with the NE quadrant coming ashore within ANWR (Blake and Zelinsky, 2018). Sustained winds were measured at 115 knots, with gusts of 126 knots, though it is likely that maximum winds were not sampled due to instrument failure at Copano Bay (Blake and Zelinsky, 2018). Storm tide measurements at ANWR reached 1.46 m MHHW (2.44–3.05 m above ground level), although high-water mark surveys suggest water levels of 3.35-3.66 m above ground level (Blake and Zelinsky, 2018) and ANWR reported 139.7 cm of rain during this event.

METHODS

Field Description and Sampling

A special use permit application for research and monitoring within the Aransas/Matagorda Island National Wildlife Refuge Complex was obtained from the US Fish and Wildlife Service for soil sampling within ANWR's Tatton Unit. Sampling occurred along two transects extending NNW from St. Charles Bay inland that contained mapped vertisols, and vertic intergrades, targeting topographic microlows without surface ponding when possible. Transect 1 was approximately 1.05 km from 28.213°N, -96.980°W and 28.224°N, -96.983°W and included five sampling sites (Fig. 1C). Transect 2 was approximately 2 km from 28.268 °N, 96.919°W to 28.286°N, 96.926°W and included four sampling sites, three of which were within the floodplain of Twin Creek (Fig. 1D). Permit 21530–19–10 was approved by the ANWR manager in Spring 2019 and extended to allow for sampling of transect 2 in 2021 as heavy rains made some planned locations inaccessible.

Soil pits were hand-excavated and described per NRCS protocols. Pit depth was limited by water table or augur refusal. Bulk soil samples (200 g) were collected at 10 cm increments for geochemical analysis, and a bucket augur was used to collect samples approximately 20 cm below the profile's base. Four oriented samples per profile were collected in electrical conduit boxes for

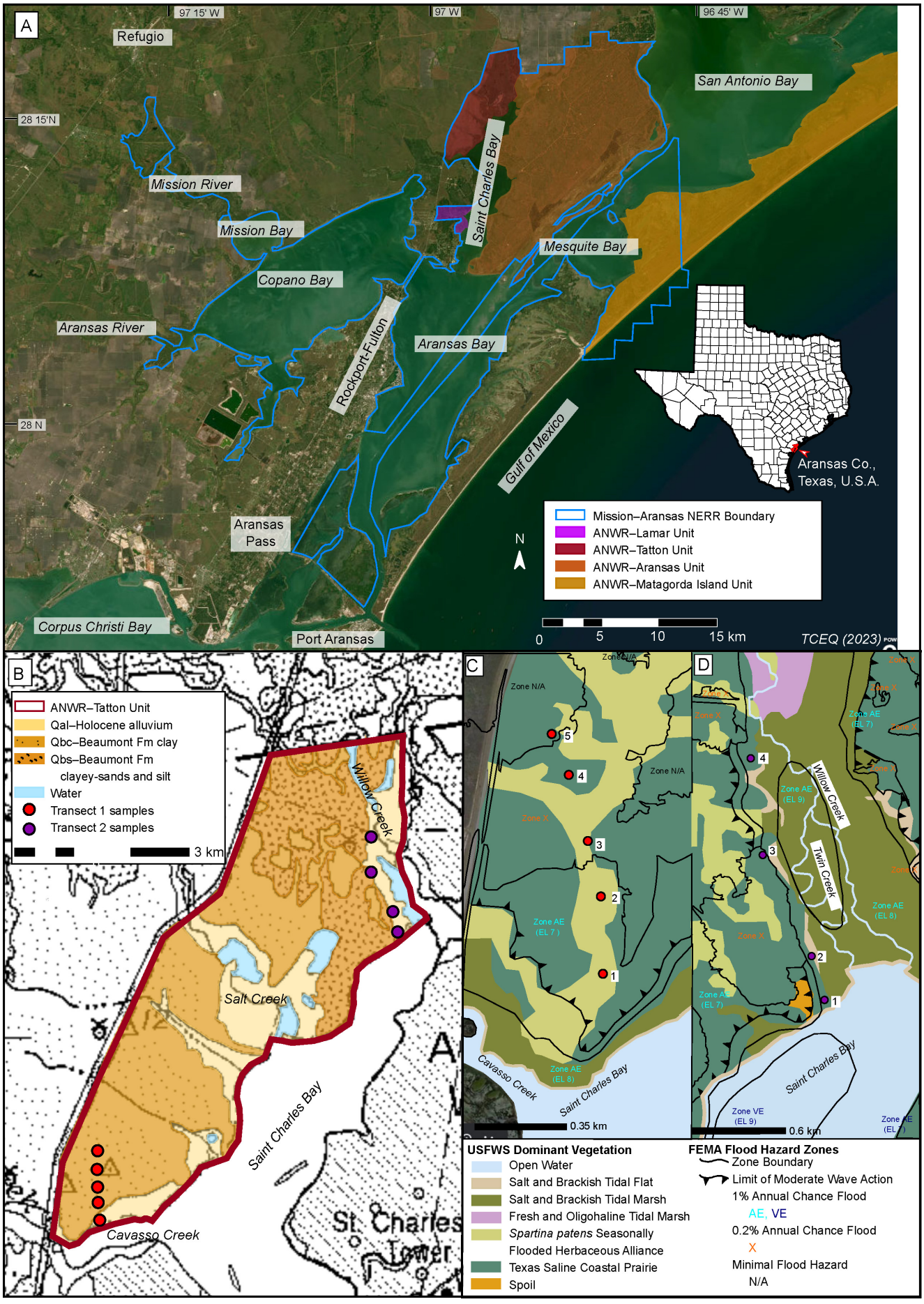
A
97 15' W
97 W
96 45' W
Refugio
San Antonio Bay
28 15'N
Mission River
Mission Bay
Saint Charles Bay
Mesquite Bay
Copano Bay
Aransas River
Rockport-Fulton
Aransas Bay
28 N
Gulf of Mexico
Aransas Co., Texas, U.S.A.
Aransas Pass
Corpus Christi Bay
Port Aransas
Mission–Aransas NERR Boundary
ANWR–Lamar Unit
ANWR–Tatton Unit
ANWR–Aransas Unit
ANWR–Matagorda Island Unit
N
0 5 10 15 km
TCEQ (2023)
B
ANWR–Tatton Unit
Qal–Holocene alluvium
Qbc–Beaumont Fm clay
Qbs–Beaumont Fm clayey-sands and silt
Water
Transect 1 samples
Transect 2 samples
3 km
Willow Creek
Salt Creek
Saint Charles Bay
Cavasso Creek
St. Charles Tower
C
Zone N/A
Zone X
Zone AE (EL 7)
Zone AE (EL 8)
0.35 km
Cavasso Creek
Saint Charles Bay
D
Zone AE (EL 9)
Willow Creek
Twin Creek
Zone VE (EL 9)
0.6 km
USFWS Dominant Vegetation
Open Water
Salt and Brackish Tidal Flat
Salt and Brackish Tidal Marsh
Fresh and Oligohaline Tidal Marsh
Spartina patens Seasonally Flooded Herbaceous Alliance
Texas Saline Coastal Prairie
Spoil
FEMA Flood Hazard Zones
Zone Boundary
Limit of Moderate Wave Action
1% Annual Chance Flood
AE, VE
0.2% Annual Chance Flood
X
Minimal Flood Hazard
N/A

(FACING PAGE) Figure 1. (A) Mission-Aransas NERR and ANWR Management Unit boundaries within Aransas County, Texas, U.S.A. (USFWS, 2010; UT–MSI, 2015); (B) geologic units within Tatton Unit, ANWR from the Geologic Atlas of Texas, Beeville–Bay City sheet (Barnes, 1987); (C) dominant vegetation and FEMA flood hazard zones along SW transect (transect 1) (USFWS, 2010; FEMA, 2016); and (D) dominant vegetation and FEMA flood hazard zones along NE transect (transect 2) (USFWS, 2010; FEMA, 2016).

Table 3. Mapped soil series within ANWR Tatton Unit, Aransas and Refugio counties, Texas (SSS, 2023).

Map Unit Symbol	Soil Series	Taxonomic Classification	% AOI Tatton Unit	% AOI Transect 1	% AOI Transect 2	Sampled Sites
As	Aransas Clay	Fine, smectitic, hyperthermic typic natraquert	11.8	12.0	60.6	1–1 2–1 2–2
BT	Barrada-Tatton Association	Barrada (49%): Fine, mixed, active, calcareous, hyperthermic typic halaquept Tatton (45%): Siliceous, hyperthermic sodic psammaquent	12.1	7.3	-	-
Na	Narta loam	Fine, smectitic, hyperthermic vertic natraqualf	26.1	68.7	22.1	1–2 1–4 2–3
RaA	Raymondville clay loam	Fine, mixed, superactive, hyperthermic vertic calciustoll	3.5	-	-	-
Va	Victine clay loam	Fine, smectitic, hyperthermic sodic haplustert	39.6	49.2	16.5	1–3 1–5 2–4
VcA	Victoria clay	Fine, smectitic, hyperthermic sodic haplustert	2.5	-	0.9	-
W	Water	-	4.9	-	-	-

micromorphological analysis, with an emphasis on horizon boundaries. The electrical conductivity (EC) of the GW was measured at each location with a conductivity meter, although ongoing rain and recent storms likely resulted in underestimates.

Laboratory and Analytical Methods

Geochemical and Wet Chemical Analysis

To determine selected major and trace elements and oxides (Ca, Fe, K, Mg, Na, Al, Si, Mn, P, Ti, and Zr), 30 g subsamples of soil were oven-dried, ground, and homogenized using a SPEX Shatterbox ring and puck mill. Soil (0.01 g) was mixed into 0.05 g of lithium metaborate flux in a platinum crucible and heated in a gas-burner fusion machine (Watanabe, 2015). A Rigaku ZSX Primus II wavelength dispersive x–ray fluorescence (XRF) analyzer analyzed the resultant glass beads. Results were reported in oxide weight percent for major oxides and ppm for trace oxides, then normalized to elemental weight percent for comparison. Bulk samples from transect 2 were consolidated by horizon for soil characterization by the Texas A&M AgriLife Research Soil Characterization Laboratory, including particle size distribution, organic carbon content, sodium adsorption ratio (SAR), calcite, dolomite, calcium carbonate equivalent, gypsum, EC, and water-soluble cations by saturated paste. The laboratory methods for these analyses are described in Soil Survey Staff (1996).

Micromorphology

Oriented samples were air-dried, and samples from three profiles per transect and thin sections were commercially prepared (n = 24). Samples were impregnated with clear epoxy resin and then cut and mounted onto 2 in x 3 in (5.1 cm x 7.6 cm) uncovered, unpolished slides with special handling due to water-sensitive material. Microscopy was conducted on an Olympus BX–51 research petrographic microscope with a 12.5 megapixel Leica digital camera and image capture software. Photomicrographs of representative soil features, and features of interest for transects 1 and 2 can be seen in Figures 2 and 3, respectively.

Clay Mineralogy

Clay mineralogy was determined at Baylor University using a Siemens D–5000 x–ray diffractometer with Cu–Kα radiation at an accelerating potential of 40 kV and a tube current of 30 mA. Samples were sonicated in 10 s intervals for 2 min to break up flocculated aggregates, then the clay size-fraction (<2 μm) was isolated via centrifuge for 3 min at 1000 revolutions per min, and the distillate was vacuum-oriented and applied to glass slides following the Millipore transfer method outlined by Moore and Reynolds (1989). Oriented aggregates were scanned over a range of 2–30° 2θ with a step size of 0.04° and a dwell time of 2 sec. Due to suspected smectite group clay minerals, samples were treated with ethylene glycol vapors in a desiccator for 24 hr, then rescanned to identify a characteristic 17 Å peak (Poppe et al., 2001).

RESULTS

Transect 1

Field Description

Environments included Central and Upper Texas Coast Salt and Brackish Tidal Marsh and Texas Saline Coastal Prairie (USFWS, 2010) (Fig. 1C) (Table 4). Vegetative covered increased inland along the transect, dominated by *Spartina* sp. and other salt-tolerant species. Patches of *Typha* sp. suggest localized ponding of fresh GW nearby. The distribution of surface water ponding from recent rain events suggested gilgai microrelief and often restricted sampling to topographic microhighs. Large anthropogenic debris including water jugs, boards, refrigerators, bottles, and plastic fragments, were observed up to 0.8 km inland.

Soils were mapped as Aransas clay, Narta loam, and Victine clay loam (Fig. 4A) (Table 3). Soils were predominantly clay, though coarse materials were incorporated as sand lenses and within burrow fills at proximal sites (Figs. 4G–4K). Coarse textures likely resulted in better drainage (Fig. 4G), but most sites were gleyed throughout, with oxidized mottles and root channels suggesting fluctuating GW. Fine carbonates were common at

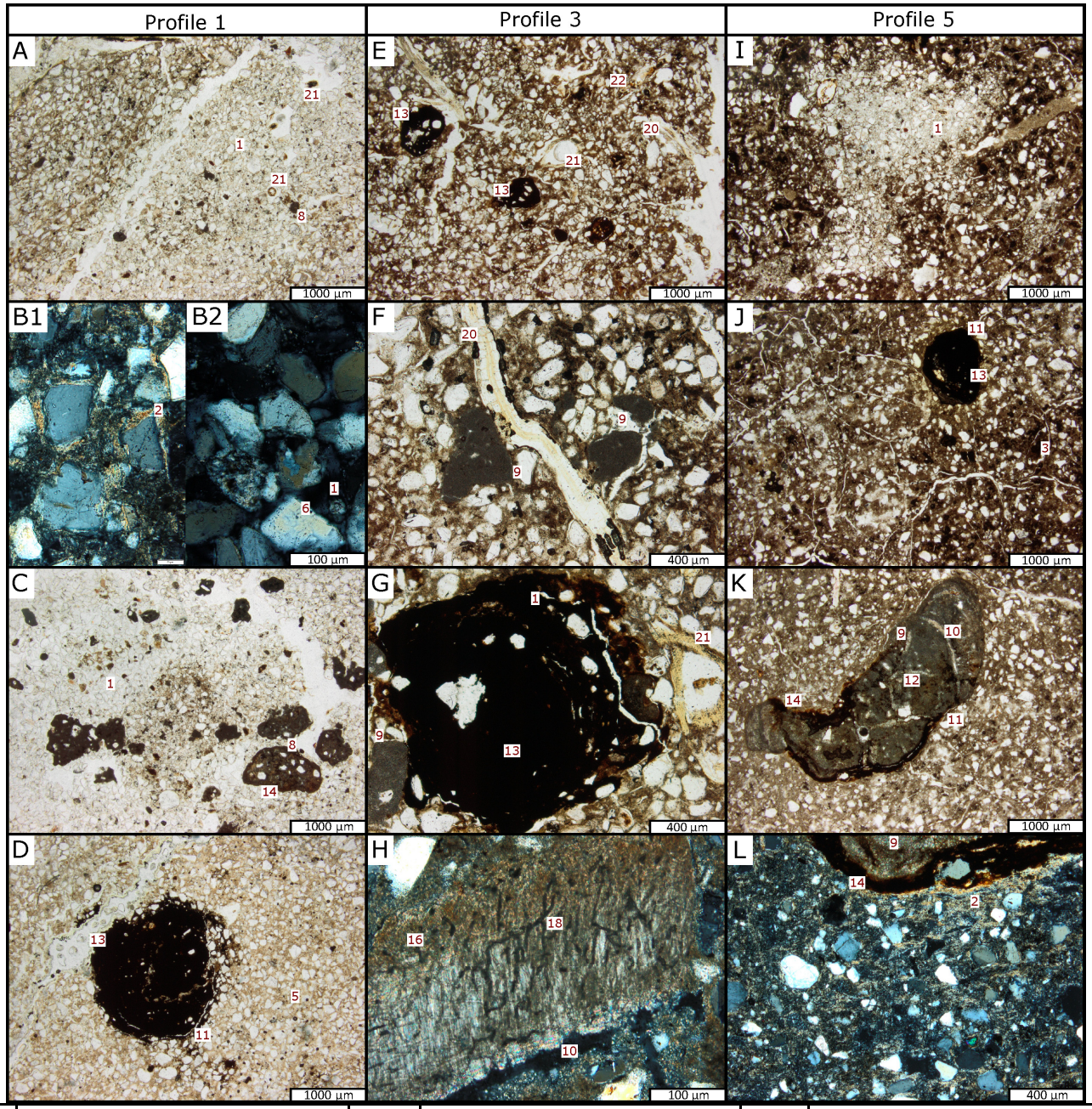

1	Coarse infills	8	Carbonate rip-up clast	16	Bivalve fragment
2	Aligned clays	9	Pedogenic micrite	17	Gastropod fragment
3	Enhanced soil structure	10	Microsparry cement	18	Borings
4	Redox enrichment	11	Circumgranular crack	19	Enhanced OM
5	Redox depletion	12	Septarian crack	20	Roots
6	Monocrystalline quartz	13	Fe–Mn concretion	21	Root cross-section
7	Polycrystalline quartz	14	Fe–Mn impregnation	22	Fecal pellets
		15	Pyrite		

Figure 2. Photomicrographs illustrating representative features and dominant processes at sites on transect 1. (A) Burrow infilled with coarse sediment, carbonate rip-up clasts, and organic material in fine soil matrix (1 cm, plane-polarized [PPL]); (B1) Aligned clays along the margin of quartz grains in soil matrix; (B2) absence of aligned clay or fine-grained sediment in burrow (1 cm, cross-polarized light [XPL]); (C) micrite-cemented, quartz-embedded clasts impregnated with Fe and Mn in burrow infill (1 cm, PPL); (D) Fe–Mn concretion in a depleted matrix (45 cm, PPL); (E) representative A horizon features including fecal pellet-lined roots, Fe–Mn concretions, and quartz grains in fine clay matrix (3 cm, PPL); (F) pedogenic micrite along root channel (35 cm, PPL); (G) Fe–Mn concretion and adjacent micrite within clay matrix (35 cm, PPL); (H) borings within recrystallized shell fragment (50 cm, XPL); (I) coarse infilling in burrow or soil crack at soil surface (3 cm, PPL); (J) increased soil pedality, weak circumgranular cracking around Fe–Mn concretion (12 cm, PPL); (K) internal cracks recrystallized to microspar in micritic carbonate nodule, Fe and Mn along external surfaces, and circumgranular cracks (58 cm, PPL); and (L) clay alignment in the soil matrix and along boundary of micrite nodule (58 cm, XPL).

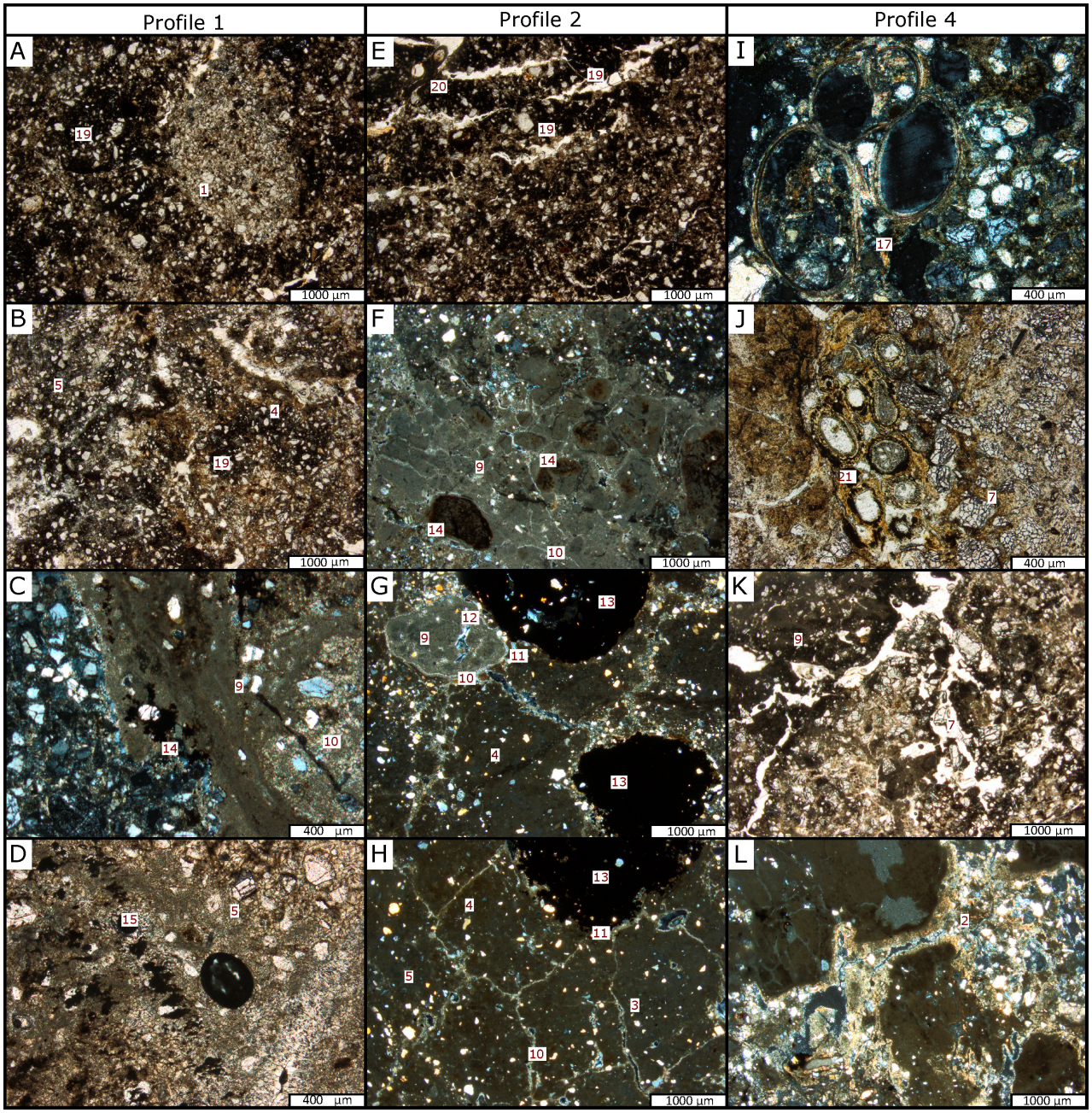

Figure 3. Photomicrographs illustrating dominant processes and representative features at sites on transect 2 (for key to identified features, see bottom of Figure 2). (A) Coarse-grained burrow infill in organic-rich fine matrix (1 cm, PPL); (B) zones of redox enrichment and depletion in soil matrix, fine-grained coating in soil cracks (18 cm, PPL); (C) boundary between carbonate-cemented zone including micrite and microspar impregnated by Fe and Mn and soil matrix with weakly aligned clays (45 cm, XPL); (D) linear axis of rhombic opaque mineral (pyrite) in fine-grained, micrite cemented matrix (45cm, PPL); (E) horizontal laminae enriched with organic matter in floodplain A–horizon (3 cm, PPL); (F) zone of micrite nodules partially cemented by microspar at nodule boundaries, some with Fe–Mn impregnation (20 cm, XPL); (G) zones of redox enrichment and depletion in fine-grained soil matrix, Fe–Mn concretions with aligned clay coatings, micritic nodule with internal cracking and circumgranular cracking around microspar boundary (37 cm, XPL); (H) improved soil structure within soil matrix, microspar cements on ped boundary and soil voids (37 cm, XPL); (I) cross-section of snail shell, partially infilled with fine-grained material (5 cm, XPL); (J) root bundle in matrix of fine-clay and agglutinated quartz burrow linings (20 cm, PPL); (K) horizontally oriented carbonate cements in fine-clay and cracked quartz matrix (35 cm, PPL); and (L) dense, flaky clay with aligned clay coatings on ped margins (60 cm, XPL).

Table 4. Environmental characterization of sampling locations.

Site Name	Distance from Coast (m)	Dominant Vegetative Community	Site Description	GW Depth (cm)	Vertic Features?
1-1	250	Central and Upper TX Coast Salt and Brackish Tidal Marsh	Exposed tidal marsh with storm deposits including surface sands and large anthropogenic debris, VL, *Spartina* sp. and *Salicornia* sp.	65	-
1-2	550	TX Saline Coastal Prairie	ML, VE, *Spartina* sp. with less than 10% broadleaf vegetation	70	Absent in profile, SW ponding pattern suggests microrelief
1-3	800	TX Saline Coastal Prairie	MH, VE, *Spartina* sp. dominant with 5% broadleaf and 5% bare ground; anthropogenic storm debris	>95	Absent in profile, SW ponding pattern suggests microrelief
1-4	1050	TX Saline Coastal Prairie	MH, VE, *Spartina* sp. dominant with bottlebrush and mesquite saplings present	>95	Weak clay alignment on pressure faces
1-5	1250	TX Saline Coastal Prairie	MH, extensively rooted, no living vegetation	>105	Slickensides, aligned clays in matrix and on ped boundaries, coarse infills
2-1	200	South TX Salt and Brackish Tidal Flat	Proximal FP of Twin Creek, VA with surficial microbial crusting	67	-
2-2	500	South TX Salt and Brackish Tidal Flat	Proximal FP of Twin Creek, VA with surficial microbial crusting	65	-
2-3	1350	*Spartina patens* seasonally flooded herbaceous alliance	MH on SS adjacent to Twin Creek, 0.3m elevation gain, VE	>105	Weak clay alignment on pressure faces
2-4	2200	Central and Upper TX Coast Salt and Brackish Tidal Marsh	Distal FP of Twin Creek, VL dominated by *Spartina* sp.	80	-

GW, groundwater; SW, surface water; ML, topographic microlow; MH, topographic microhigh; FP, floodplain; SS, sandsheet; outside FP of Twin Creek; VE, extensive vegetation; VL, limited vegetation; and VA, vegetation absent.

proximal sites, increasing in size and cementation inland. GW was brackish at proximal sites, and gypsum precipitated out of the GW at 1–2 (Fig. 4H). Despite all soils being mapped as vertisols or vertic intergrades, there was only evidence of vertic features in 1–4 (as mm–scale pressure faces between peds) and 1–5 (as coarse-filled macropores and slickensides increasing in size and definition with depth below 40 cm) (Figs. 4J and 4K). Complete field descriptions for each soil profile are included in Appendix.

Micromorphology

Clay content increased with depth and distance from the coast, with 1–1 having burrow infills of translocated coarse-grained materials, including quartz sand and carbonate rip-up clasts (Figs. 2A–2C). Other carbonate forms included micritic nodules forming along root traces (Fig. 2F) and micritic nodules recrystallized to microspar in internal cracks (Fig. 2K). Fe or Mn partially impregnated many carbonate nodules, suggesting fluctuating redox conditions (Figs. 2K and 2L). Other redox features included matrix gley and zoned ferromanganese concretions up to 2 mm in size (Figs. 2D and 2G). Evidence of biotic activity included roots (Figs. 2E and 2F) and other plant material, fecal pellets (Fig. 2E), and bored bivalve fragments (Fig. 2H). Vertic features were present in 1–5, including circumgranular and septarian shrinkage cracks and subangular blocky to wedge-shaped peds (Fig. 2J). Coarse infills were also seen in surface cracks at 1–5 (Fig. 2I). Clay alignment is present as pressure faces along quartz sand grains and on coarser soil features (Fig. 2L).

Bulk Oxide Geochemistry

Sodium oxide (Na_2O), normalized to Na^+, decreases with distance from the coast and increases with depth, with concentrations at proximal sites exceeding distal sites at most depths (Fig. 5A1). Depth trends for calcium oxide (CaO), normalized to weight percent Ca^{2+}, vary with distance from the coast, generally increasing at distal sites, and decreasing at proximal sites (Fig. 5B1). Ca^{2+} increases with distance from the coast, and intraprofile variability is greatest at distal sites. Magnesium oxide (MgO), normalized to weight percent Mg^{2+}, increases with depth at all sites to approximately 20 cm, then stabilizes (Fig. 5C1), with lower B–horizon concentrations increasing consistently with distance from the coast. Depth trends for phosphorus (normalized from P_2O_5) decrease with depth at proximal sites, whereas concentrations at distal sites are elevated at the surface, then decrease slightly to approximately 20–30 cm (Fig. 5D1). Phosphorus increases somewhat with distance from the coast. Potassium oxide (K_2O), normalized to K^+, increases to approximately 20–30 cm, then decreases to the base of the profile (Fig. 5E1) and increases with distance from the coast. Patterns of SiO_2 and Zr mirror each other, generally decreasing with depth (Figs. 5F1 and 5G1) and distance from the coast. Patterns of Al_2O_3 and Fe_2O_3 mirror each other, increasing with depth to about 20–30 cm and then decreasing to the base of each profile (Figs. 5H1 and 5I1). Surface concentrations are lowest at 1–1 and highest at 1–5, but deeper in the profile, concentrations increase with distance from the coast. Geochemical trends are summarized in Table 5.

Clay Mineralogy

X–ray diffractograms in Figure 6 show stratigraphic variations in B–horizon clay mineralogy with distance from the coast. X–ray patterns were processed by MDI JADE to identify peak positioning and interlayer spacing and compared against published values in the program library. Most samples were dominated by broad, low-angle peaks that often contained or obscured a low-angle-side shoulder 10 Å reflection peak of illite that became sharper and more symmetrical after glycolation. Secondary illite reflections were present as shallow 5.0 Å peaks. Untreated peaks exceeding 15 Å that shifted to approximately 17.0–17.5 Å after ethylene glycol solvation were identified as smectite; peaks that

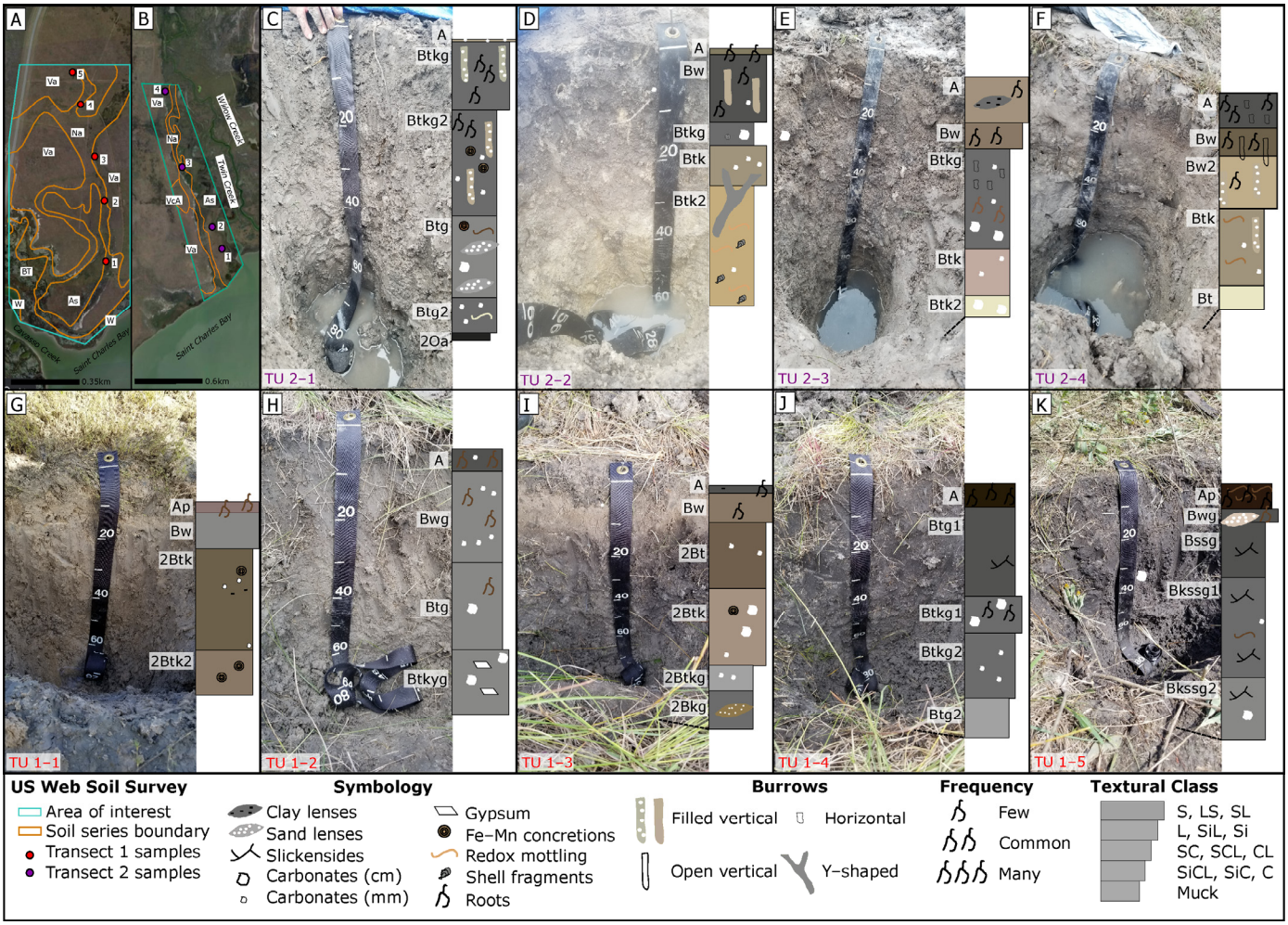

Figure 4. (A) Mapped soil series within transect 1; (B) mapped soil series within transect 2 (SSS, 2023; explanation in Table 1); (C–F) soil profile photographs and interpretations on transect 2, 200, 500, 1350, and 2200 m from St. Charles Bay; and (G–K) soil profile photographs and interpretations on transect 1, 250, 550, 800, 1050, and 1250 m from St. Charles Bay.

did exceed 15 Å in untreated samples that adjusted to values greater than approximately 18 Å were interpreted to be mixed-layer illite-smectites (I/S) (Patarachao et al., 2019). Broad peaks with d–spacing ranging from 19.5–22.0 Å in untreated samples that adjusted to approximately 17.5 Å after glycol solvation were interpreted to be poorly ordered smectites, whereas those that shifted to approximately 18 Å were interpreted as poorly-defined mixed I/S. Kaolinite was present at all sites in 7.18 Å peaks at 12.5° 2θ and 3.58 Å peaks around 25° 2θ. Quartz also made up a major component of the clay-size fraction of ANWR samples and can be seen as sharp 3.34 Å peaks at 26.6° 2θ.

Transect 2

Field Description

Most transect 2 sampling sites were within the floodplain of Twin Creek, with 2–3 located approximately 0.3 m above the floodplain on a sandsheet (Table 4). Environments included South Texas salt and brackish tidal flat, *Spartina patens* seasonally flooded herbaceous alliance, and Central and Upper Texas Coast salt and brackish tidal marsh (USFWS, 2010) (Fig. 1D). Proximal floodplain sites were unvegetated and contained microbially cemented organic layers interlayered with sands in the uppermost portion of the soil, indicating frequent fluctuations in surface water. Vegetation was most extensive at 2–3, though *Spartina* sp. and other salt-tolerant species were also present at 2–4. Evidence of insects, mollusks, and vertebrates (birds) along the floodplain included trackways, trails, shell debris, and living organisms on the soil surface. Soil profiles were highly bioturbated, with well-developed burrows including infilled, open vertical, open horizontal, and infilled Y–shaped morphologies (Figs. 4C–4F).

Soils along transect 2 were mapped as Aransas clay, Narta loam, and Victine clay loam (Fig. 4B) (Table 1). Proximal soils had coarse surface horizons, sand-filled burrows in a clay matrix, and often included microbial textures at the surface with laminated mineral and organic layers (Figs. 4C and 4D) (Appendix). Evidence of a buried A horizon at the base of 2–1 included a mucky consistency, dark color, and hydrogen sulfide odor (Fig. 4C). Compared to the other sites, 2–3 had improved soil structure, better-defined carbonate nodules, and limited matrix gley, suggesting better drainage (Fig. 4E). Limited redoximorphic gleying at 2–4 also suggested better drainage versus the proximal floodplain. Still, carbonates were limited, and soil structure was either weak or secondarily destroyed by bioturbation, suggesting frequent flooding (Fig. 4F).

Micromorphology

Biotic activity was more prevalent along transect 2, including coarse-infilled burrows (Fig. 3A), burrows lined with agglu-

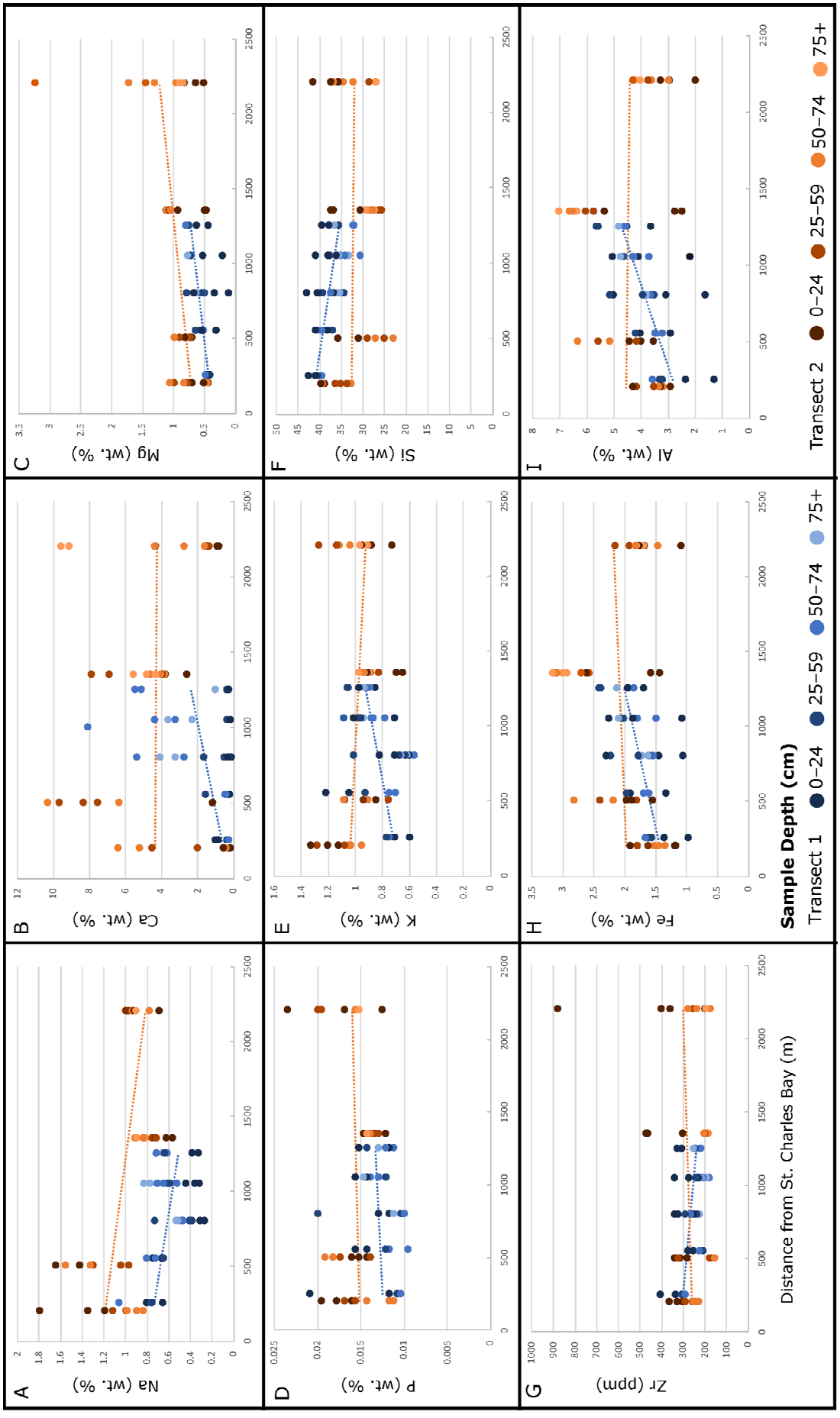

Figure 5. Geochemical trends (elemental weight percent) vs. profile depth for transects 1 and 2 for selected major oxides; EC, SAR, and ESP vs. depth for transect 2.

Table 5. Proposed explanations for geochemical trends with distance and depth on transect 1.

Element/ cation	Depth Patterns	Proximal-Distal Patterns	Possible Explanation
Na	Increase	Decrease	Brackish GW; SW additions in 1–1; rainfall dilution and enhanced leaching at distal sites
Ca	Increase	Increase at >40 cm	ET and formation of pedogenic carbonate, marine bioclasts
Mg	Increase in all except 1–1	Increase	Brackish GW, SW additions in 1–1, marine bioclasts
P	Decrease	Slight Increase	SW with elevated P, vegetative demand
K	-	Increase	Vegetative demand
Si	Decrease	Decrease	Surface additions of tempestite detrital silicates
Zr	Decrease	Decrease	Dry deposition of aeolian deposits, tempestite detrital silicates
Al	Increase	Increase	Al_2O_3 in clay minerals countered by SiO_2 and Zr additions at proximal sites, upward mobilization of acid cations at when exposed to seawater (Wong et al., 2015)
Fe	Increase	Increase	Surface saturation favors iron reduction and leaching soluble iron through profile; tempestite silicates comparatively low in iron

GW, groundwater; and SW, surface water.

tinated sand grains (Fig. 3J), roots and other plant materials (Fig. 3J), and gastropod shell fragments (Fig. 3I). Microbial textures were present in the uppermost portion of 2–2 (Fig. 3E). Soils contained mixtures of fine-grained clays and coarse-grained monocrystalline quartz grains (Fig. 3I), and clay content increased with depth. Strongly developed vertic features were not observed, but clay alignment on the margins of larger fine-grained aggregates in 2–4 suggested a change in clay chemistry (Fig. 3L); an abrupt transition to heavy white clay at the base of 2–3 and 2–4 supports this interpretation. Carbonates included isolated nodules of pedogenic micrite, sometimes with microspar coatings or internal cracks (Fig. 3G), microspar cement along ped boundaries (Fig. 3H), and partially cemented, multi-nodular pedogenic micrite (Fig. 3F). Many carbonate features were partially impregnated by Fe and Mn, suggesting fluctuating redox conditions (Figs. 3C and 3F). Other redox features included zones of matrix gley (Fig. 3B) and the formation of zoned ferromanganese concretions up to 2 mm in size (Fig. 3G). Rhombohedral pyrite was present in the lower portion of 2–1 (Fig. 3D).

Bulk Oxide Geochemistry

Patterns of Na^+ with depth vary by site, but generally decrease with distance from the coast. Surface concentrations are highest on the proximal floodplain, decreasing with depth at 2–1, and increasing beyond 30 cm at 2–2 (Fig. 5A2). The surface is depleted at 2–3 and concentrations resemble transect 1, while concentrations do not vary with depth at 2–4. At all sites, Ca^{2+} increases with depth, but does not show consistent trends with distance from the coast. Surface concentrations are highest at 2–3 and increase with distance from St. Charles Bay along floodplain sites (Fig. 5B2). Concentrations of Mg^{2+} increase with distance from the coast and increase with depth at most sites (Fig. 5C2), though increases may appear as pulses. P concentrations decrease with depth at the proximal sites, whereas more inland sites have depleted surfaces (Fig. 5D2). Concentrations of P increase slightly with distance from the coast, with the floodplain being enriched relative to the sandsheet, which has concentrations similar to transect 1. K^+ appears to converge with depth at all sites; surface concentrations are highest on the proximal floodplain and decrease with distance from the coast, but at most depths, all floodplain sites are enriched relative to the sandsheet (Fig. 5E2). Depth trends for SiO_2 and Zr are somewhat contradictory, especially in the floodplain (Figs. 5F2 and 5G2). Patterns at 2–3 are similar to transect 1, with enrichment at the surface and a corresponding decrease with depth, whereas 2–4 has pulses of enrichment around 20 and 70 cm. SiO_2 and Zr concentrations do not appear to vary with distance from the coast. Al_2O_3 and Fe_2O_3 increase with depth, most dramatically at 2–3 (Figs. 5H2 and 5I2), and have little variability with distance from the coast, although all samples from 2–1 and 2–4 are lower than the transect 2 average. Geochemical trends are summarized in Table 6.

Soil Characterization

Ammonium acetate-extractable bases (meq/100 g) were used to calculate exchangeable sodium percentage (ESP) horizon by horizon for transect 2 (Fig. 5). At all depths, for all profiles, soils meet the criteria for saline-sodic (Table 1). EC decreased with depth at all sites, decreased slightly with distance along the floodplain, and was enriched in the floodplain relative to the sandsheet. SAR decreased with depth at proximal sites, decreased with distance along the floodplain, and was lowest on the sandsheet. ESP slightly increased with depth at most sites and was elevated at 2–1 and 2–3. Elevated calcite (13.3–21.0%) within the B–horizons of 2–2 likely contributed to reduced ESP at that site.

DISCUSSION

Pathways of Marine Influence at ANWR

Groundwater

Slightly-to-moderately saline shallow GW is one source of salinization of the Tatton Unit (Fig. 7). Within the GW, wet-deposition of marine aerosols concentrated by high ET, halite dissolution, brine migration (Chowdhury et al., 2018), and SI (Chowdhury et al. 2006) contribute to salinity. EC of seeped GW ranged from 48 mS/cm at upland sites to 89.2 mS/cm in the floodplain, exceeding drinking water standards and recommended values for irrigation water (Fipps, 2021). The depth to GW increased with distance from the coast from 65–70 cm to greater than 105 cm on transect 1 (Table 4); although heavy rainfall during sampling obscured GW seepage for transect 2, oxidized mottling in a depleted matrix suggested water table fluctuations at 71–80 cm. Micromorphological features indicate water table fluctuations within 1 m of the soil surface at many sites, whereas pyrite forming at 2–1 indicates prolonged saturation (Fig. 3D).

Upward diffusion of saline groundwater due to ET and vegetative demand enhances salinization in the rooting zone

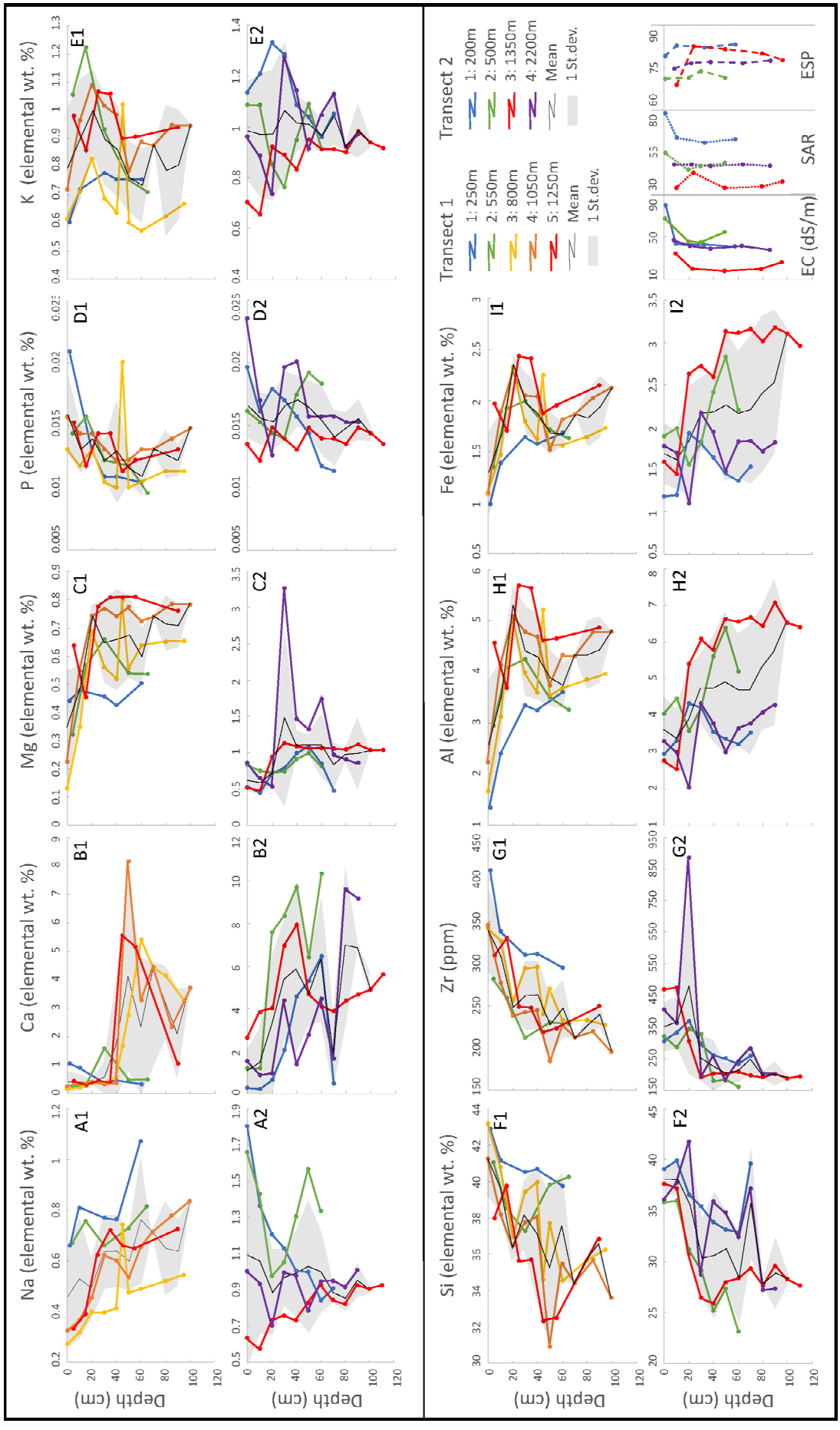

Figure 6. X–ray diffractograms from B horizons in 1–1, 1–3, and 1–5. Untreated oriented aggregates are blue, oriented aggregates saturated with ethelyne glycol are orange. Minerals are labeled: S–smectite, I–illite, I/S–interstratified illite/smectite, aS–poorly defined smectite, aI/S–poorly defined interstratified illite/smectite, K–kaolinite, Q–quartz. Note scale differences on intensity counts.

Table 6. Proposed explanations for geochemical trends with distance, depth, and landscape position on transect 2.

Element/ cation	Depth Pattern	Proximal-Distal Pattern	Landscape Position Pattern	Possible Explanation
Na	Decrease, except SS	Decrease	FP enriched vs. SS; SS surface depletion	Brackish GW, tidal surface additions in proximal FP
Ca	Increase	-	SS elevated at surface vs. FP	ET and pedogenic carbonate, translocated marine bioclasts from storm deposits
Mg	Increase	Increase	-	Brackish GW
P	Decrease	Slight Increase	FP enriched vs. SS	SW with elevated P, vegetative demand higher on SS
K	Decrease	Slight Decrease	FP enriched vs. SS	Vegetative demand higher on SS, increased landscape stability and K-feldspar weathering
Si	Decrease	-	-	Tempestite detrital silicates at proximal and FP sites, sediment pulses from freshwater flooding events
Zr	Decrease	-	SS surface enriched vs. FP	Dry deposition of aeolian deposits, tempestite detrital silicates at proximal sites, loss of fines during flood events along FP
Al	Increase	Slight Increase	SS depleted at surface, enriched at depth vs. FP	Clay content reduced by SiO_2 and Zr additions, increased landscape stability beyond levee, upward mobilization of acid cations exposed to seawater (Wong et al., 2015)
Fe	Increase	Slight Decrease	SS depleted at surface, enriched at depth vs. FP	Surface saturation favors soluble iron and leaching through profile, SiO_2–rich surface additions have less iron
EC	Decrease	Decrease at surface	SS depleted vs. FP	Rainfall reduces EC at surface, brackish GW, tidal influence on FP
SAR	-	Decrease	SS depleted vs. FP	Tidal and storm inputs at proximal sites, FP
ESP	Slight increase	-	Surface depletion in SS vs. FP	Rainfall reduces surface ESP, greater depth to GW on SS, increased tidal influence on FP

FP, floodplain (brackish-to-saline tidal flat, tidal marsh, Texas saline coastal prairie within FEMA Flood Zone AE and Limit of Moderate Wave Action); SS, sandsheet (Texas Saline Coastal Prairie, FEMA Flood Zone X); GW, groundwater; and SW, surface water.

(Rengasamy, 2006). In many profiles, the depth to carbonate horizons was shallower than expected due solely to pedogenesis, supporting a GW source of Ca^{2+} (Royer, 1999). At some sites, micritic carbonate nodules were horizontally cemented by micrite, also suggesting GW alteration rather than a purely pedogenic origin (Fig. 3F). Geochemical trends for Na^{+} also support GAS, with increases with depth at upland sites and decreases with depth along the floodplain; apparent convergences in concentrations of Na^{+} and Mg^{2+} deep within the profiles suggest that these differences can be attributed to reduced surface additions further from the coast, rather than changes in GW chemistry (Figs. 6A and 6C). Trends in soil EC support this, with EC decreasing with distance from the coast at the soil surface but remaining similar at depth (Fig. 5).

Surface Additions

Sources of surface salinization include additions of brackish tidal water and sediments along floodplain channels and storm deposits at all sites, although they are likely somewhat countered by pulses of freshwater additions from rain events. Tidal influence is most evident in the proximal floodplain, but the increased importance of surface additions can be seen geochemically at all floodplain sites relative to upland sites. This is most evident for Na^{+} (Fig. 5A2), but surface additions from St. Charles Bay, which has concentrations of P between 0.02–0.16 mg/L (West and Wetz, 2021), may contribute to elevated P in the floodplain versus upland sites (Fig. 5D2). A thin surface horizon of thinly laminated microbially cemented organics and sands was visible in the field and in thin-section at 2–1 and 2–2, suggesting tidal deposition (Fig. 3E). Elevated EC, SAR, and ESP at the soil surface within the proximal floodplain also indicate frequent surface additions (Fig. 5J). Similar patterns of ionic abundance for Na^{+}, K^{+}, Mg^{2+}, and Ca^{2+} as well as Cl^{-} and SO_4^{2-} was observed in coastal saline soils in Senegal, showing increased marine surface inputs seaward and the greater effects of tidal inundation and capillary rise from saline GW in more inland locations, as well as, increased marine influence in floodplain soils versus fluvial terraces (Fall, 2017).

Hurricane Harvey likely deposited recent debris along transect 1; patterns of coarse sediments observed in soil profiles, photomicrographs, and geochemical trends support tempestite additions at the soil surface. Proximal upland sites had coarse-grained wavy horizons or broken lenses, and burrow infills at upland and floodplain sites were often coarser than the surrounding matrix (Figs. 2A, 2B2, 2I, and 3A). Carbonate fragments interpreted to be tempestite rip-up clasts were also present in burrow infills at 1–1 (Fig. 2C). Geochemical trends for SiO_2 and Zr support a tempestite origin for sands and silts at the upland sites, with surface concentrations decreasing with distance from the coast. The lack of relationship between distance and SiO_2 or Zr concentrations suggests that coarse-grained sediments may have been carried landward well beyond the transect along the floodplain channel. Sedimentary evidence of Hurricane Harvey, including deposits of inorganic sands and muds, was present up 10 km inland along fluvial channels at the San Bernard National Wildlife Refuge, approximately 210 km NE of ANWR, and Cl^{-}/Br^{-} ratios support SI along channels in the absence of sedimentary evidence (Yao et al., 2019).

Rain events also introduce freshwater pulses to ANWR, with heavy rains predating and concurring with sampling in 2019 and 2021, resulting in standing water throughout the reserve and flowing water in Twin Creek. In 2021, 40.46 cm of rainfall occurred in Rockport, when the seasonal average for March, April, and May is 18.57 cm. Enhanced leaching associated with freshwater pulses can be seen as decreased Na^{+} with depth in upland sites on both transects and decreased surface ESP and SAR on the sandsheet relative to the floodplain. Additionally, large fluctuations in Si and Zr and associated decreases in Na^{+}, P, K^{+}, Al_2O_3, and Fe_2O_3 at 2–4, may relate to upstream flooding within

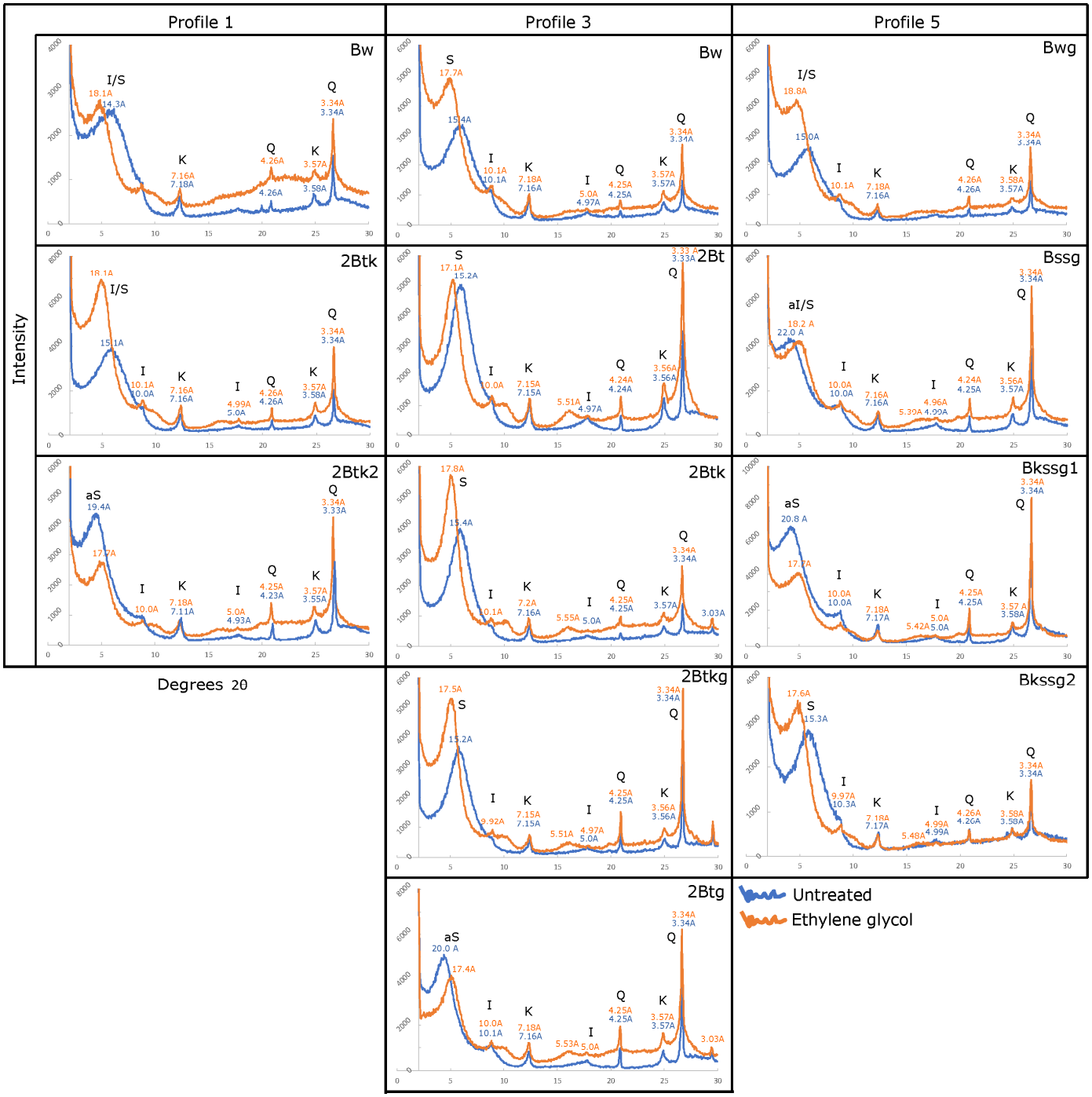

Figure 7. Sources of primary salinization of soils forming within a low-energy tidal estuarine system under current and future climate scenarios (modified after Rotzoll and Fletcher, [2012], Daliakopulous [2016], and Tully et al., [2019]).

the channel of Twin Creek (Fig. 5). Zr is also depleted on the floodplain surface relative to the sandsheet, which could be the result of the stripping of the silt size-fraction during flood events.

Where are the Vertisols?

The diagnostic morphogenetic properties of vertisols (desiccation cracks and slickensides within 100 cm of the soil surface) form as clays with a high coefficient of linear extensibility experience annual changes in water availability; and are enhanced by maximum changes from wet to dry states (SSS, 1999). Although soils on both transects are mapped as vertisols or vertic intergrades and the distribution of surface water ponding suggested gilgai microrelief, macroslickensides were only observed field at 1–5. Vertic features, including aligned clays within the soil matrix and along ped boundaries, and coarse fragments were also visible in thin sections (Fig. 2L). Weak clay alignment on pressure faces between peds occurred in 1–4 and 2–4. The base of these profiles was above the water table, although micromorphological evidence of circumgranular and septarian cracks within carbonate nodules supports fluctuations in water availability (Fig. 2K). Clays were predominantly smectite or mixed I/S, with minor components of illite and kaolinite. The relative peak heights of quartz and I/S do not appear to change with depth or distance

from the coast, despite increases in Al_2O_3 and decreases of SiO_2 with depth (Fig. 6). The XRD pattern for smectite is best developed at 1–3, which did not show any macroscale or micromorphological evidence for shrink-swell. Based on these observations, we expect that some combination of water availability and soil sodicity may restrict the formation of vertic features in smectitic soils.

The hydropedological behavior of vertisols shifts with water availability. Preferential drainage occurs along soil cracks, at the surface, and internally when rainfall or spray irrigation seals surface cracks (Kurtzman et al., 2016). In dry soil, crack density, and size decrease exponentially with depth (Kutilek, 2001). Despite higher moisture content, cracks are often deeper in microlows but form more rapidly and extensively in corresponding micro-highs (Kishne et al., 2009). Increased infiltration may also occur along macro-slickensides, intersecting arcuate features formed as differences in moisture availability within a profile form pressure differentials along areas of dilation and incomplete collapse (Nordt et al., 2004). Slickenside development is limited by overburden pressure and depth of seasonal desiccation (Blokhuis, 1982; Kutilek, 2001); if the seasonal average water table is less than 50 cm, overburden pressure may be insufficient to form macro-slickensides; however, poorly developed slickensides have been observed between 35–50 cm (SSS, 1999). Maximized changes from wet to dry states enhance shrink-swell behavior (SSS, 1999). Most swelling occurs at matric potentials between -0.3 and -15 bars, outside of which, water loss results from air entering very large soil voids or domains between Ca–saturated clays (Virmani et al., 1982). As vertisols are saturated, the pore-size distribution shifts, with an increase in fine and ultrafine intrapedal pores relative to macropores, resulting in lowered hydraulic efficiency due to the reduction in effective radii; alterations in porosity are even more dramatic when vertisols have high ESP and low concentration of soil water (Kutilek, 2001). Vertisols typically form in areas with seasonal precipitation; however, vertic features also form in high MAP soils where differential moisture statuses with depth are attributed to seasonal high ET (Kovda, 2020). In udic environments along the Texas Gulf Coast where vertisols are forming on the Late Pleistocene Beaumont Formation, gilgai microtopography and gilgai were present during field samplings, as were crack infills. Still, open cracks were not (Nordt et al., 2004). Some vertic intergrades are classified due to having the correct clay content for potential pedoturbation despite showing little or no evidence of soil movement. They do not experience sufficient variations in moisture availability in a normal year (SSS, 1999).

Shrink-swell behavior changes in response to soil and GW salinity, particularly in montmorillonitic clay soils, due to aggregate dispersion, clay illuviation, and increases in bulk density (Carroll and Starkey, 1958). Salts concentrating on clay-exchange sites, especially when soil water has lower concentrations of salts, cause soil aggregate breakdown as fine particles slake off and lodge in smaller pores, increasing non-conductive porosity, with these effects more prevalent in smectites than kaolinites and micas (Rolston et al., 1984). Clay dispersion can form crusts at the surface or subsurface, restricting both infiltration and hydraulic conductivity (Shahid et al., 2018). This is seen in thin-section as (1) a platy, clay-rich surface seal with low porosity above a coarser-grained, highly porous layer; (2) alternating layers of low and high density; (3) clay coating in and around soil voids; and (4) calcite coatings in voids and on ped surfaces (Shahid and Jenkins, 1992). Patterns of surface cracking may shift towards fewer, larger cracks and larger peds because Na^+ increases are greater relative to other cations (Blokhuis, 1982). At the same clay content and ESP, increases in electrolyte concentration decreases shrink-swell potential (Nayak et al., 2006). Volume compression and swelling indices of montmorillonite-rich clays decreased in salt solution, and clay fabric, examined using SEM, changed from thin platelets to bulky pellets. In contrast, 1:1 kaolinitic clays remained structurally stable (Zhang and Wang, 2019). This suggests saline-brackish GW could restrict shrink-swell features through the dispersion and destruction of soil structure beyond what is expected from saturation alone.

Potential Responses of Soil Salinization Pathways to Climate Change?

Changes in soil salinization pathways in response to climate change can be broadly grouped into: (A) the effects of direct marine and tidal influence through sea level rise, (B) the effects of potential drought and evaporation due to rising land and sea surface temperatures, and (C) the effects of increasing extreme precipitation events (Fig. 7), and (D) increased anthropogenic salinization through increased utilization of marginal quality GW.

Direct Marine Inundation

Globally, the rates of SLR from instrument and proxy data increased above preindustrial levels by 1863 CE, with rates from 1940–2000 exceeding all previous 60 yr intervals (Walker et al., 2022). Rates of SLR on the Texas Gulf Coast ranged from 1.2 to 4.3 mm/yr depending on variations in local topography and subsidence, exceeding the global rate of 1.4 ± 0.2 mm/yr; (Walker et al., 2022; Runkle et al., 2017). The measured SLR from the Rockport, TX tidal gauge was 5.77 ± 0.49 mm/yr from 1937–2019 (NOAA, 2020). Between the 1950s and 2004, SLR converted low tidal flats and estuarine marshes into open water and seagrass environments and to the marsh vegetation expansion into upland habitats around St. Charles Bay (Tremblay et al., 2008). SLR projections range from 0.86 to 2.84 m by 2100 (Runkle et al., 2017). Vertical accretion rates of 4.8 mm/year suggest that ANWR's Blackjack Peninsula is unlikely to be inundated soon (Callaway et al., 1997). However, lower topographic gradients in ANWR's Lamar Peninsula favor environmental shifts, with projected loss of salty prairie and grasslands and expansion of estuarine emergent environments at 1 m of SLR, and a near-total transition to unconsolidated shoreline and open water at 3 m of SLR (March and Smith, 2012). In the Tatton Unit, the NOAA SLR Viewer tool indicates that direct marine inundation will be restricted to the coastline and the flood plains of Twin, Salt, and Cavasso Creeks under 1 m of SLR, whereas 3 m of SLR results in near complete inundation.

Tidal Influence

With SLR, the extent of tidal influence is expected to extend further inland, with low-gradient tidal streams acting as conduits of marine water and sediments beyond the coast. In microtidal mixed estuaries, coastal geometries formed from interactions between river inputs and tides result in greater water-level variations between tidal creeks and bays, dampening tidal signals and the effects of currents, waves, and storm surges (Alizad et al., 2018). The Mission-Aransas Estuary system is particularly complex due to its micro-tidal range, complex tidal signature, small baseflow, and pulses of high stormflow (Jones et al., 2019). In the Aransas River, brackish water intruded 11.8 km from the river mouth and varied with baseflow, although this is likely further than in creeks with seasonal flow; however, tides also influence river hydrology beyond the extent of brackish water in the tidally influenced freshwater zone, a river segment that experiences bidirectional discharge (and therefore marine sediment inputs) and tidally controlled water stages (Jones et al., 2020).

Temperature, Drought, and Evaporative Demands

Texas is expected to warm under all future climate projections (Runkle et al., 2017). Regional drought assessments predict that increased temperature and evaporative demand will drive

droughts in the first half of the 21st century. In contrast, in the second half of the 21st century, droughts will be driven by reduced precipitation and increased ET (Hernandez and Uddameri, 2014). From 1986 to 2020, drought indices calculated from vegetation conditions and precipitation did not indicate drought at ANWR. However, the temperature condition index indicated a significant increase in land temperature and potential for drought associated with increased evaporation (Porritt, 2021), and palustrine marshes have converted to uplands due to development and long-term drought (Tremblay et al., 2008). On land, shallow GW can buffer plant stress temporarily, but ultimately surface–GW models suggest reductions in subsurface aquifer storage, especially in humid regions (Condon et al., 2020). Increased evaporative effects due to increasing SST in the Gulf of Mexico and associated estuaries and bays may result in increased salinity (Hoegh-Guldberg et al., 2014). However, open water salinity in the Mission-Aransas estuary was not linked significantly with drought from 2007–2020 (Porritt, 2021).

Storm Events, Storm Flow, and Storm Surge

Climate models using higher-end emissions scenarios anticipate the Texas Coastline will experience increased frequency and intensity of extreme precipitation events (Runkle et al., 2017; Kloesel et al., 2018). Compared to 1981–2000, by 2100, models project a sixfold increase in Harvey-like events in Texas (Emanuel, 2017). Low atmospheric pressure associated with large storm events can result in unusually high tides and large waves, leading to marine inundation from temporary SLR and wave runup (Barnard et al., 2014). Increased wind speeds and wave activity associated with storm events also generate sea spray droplets, atmospheric residence time varies by particle size, with larger diameter particles being deposited in seconds to minutes and leading to local effects. In comparison, smaller particles are transported into the atmosphere, where they may remain for hours to days (Veron, 2015). Thus, sea spray from storm events may increase coastal salinity directly and indirectly as deposits in upstream catchments may increase salinity in the GW and surface water with increased runoff. Pulses of precipitation from storm events may increase GW levels in shallow, perched saline aquifers but can also cause temporary increases in fresh GW (Hoover et al., 2017) due to direct infiltration and overland and GW flow from upslope areas (Swarzenski et al., 2017). Periodic freshwater inputs may temporarily mitigate trends in increased ionic strength, particularly Na^+, in ecosystems experiencing droughts; however, despite periods where ionic strength returns to near freshwater levels, ecosystem "memory" may result in quicker alkalinization and sulfidification during subsequent saltwater inundations (Tully et al., 2019b). Because typical stormflow within the Mission-Aransas NERR exceeded baseflow by nearly three orders of magnitude between 2015 and 2017 (Jones et al., 2019), the relative importance in stormflow will likely increase in the future.

Anthropogenic Salinization

Increased water needs due to projected population increases in Aransas County, ranging from -6.5% 2010 values by 2050 in a zero net-migration scenario to 13.5% if migration rates remain equal to 2000–2010, may result in expanded use of marginal quality wells (Hoque et al., 2014). Historically, this area of South Texas is unfavorable for freshwater development due to high Cl^- concentrations and zones of moderately saline water underlying Copano and St. Charles Bay; however, given economically feasible desalinization, the moderately saline waters are potentially extractable (Shafer, 1970). The Gulf Coast Aquifer is considered a relatively stable feedstock of brackish GW for moderate-sized desalinization plants, though secondary treatment may still be required to meet drinking water standards (Chowdhury et al., 2018). Within the boundaries of the Tatton Unit, there are records of five wells within the Texas Water Development Board's GW database: two are unused for oil and gas exploration, two are unused for water withdrawal, and one was used historically for water withdrawal for stock; with an additional two stock wells directly across Highway 35N from the Tatton Unit (TWDB, 2023). This could lead to localized SI into otherwise slightly to moderately saline GW.

Pedogenic Processes and Climate Change at ANWR

Based on observations and the understanding of soil formation processes, we hypothesize that there are two potential end-member scenarios for pedogenesis in vertisols as soil salinization pathways at ANWR respond to climate change.

Salinization Due to Saturation

In floodplain and near-coast upland soils, rising water tables and potential surface inputs from direct marine inundation, tidal influence, and freshwater flooding from storm events may increase water availability and decrease seasonality, reducing vertic properties and salinization at the soil surface. In this scenario, rising saline-brackish GW increases water availability within the profile throughout most of or all of the year, leading to expansion in swelling clay soils and shifts in drainage pathways, while additions of surface water may result in soil expansion and crack closure at the soil surface, further decreasing hydraulic conductivity. Reduced differences in hydraulic gradients within soil zones would further restrict shrink-swell potential, particularly if the top of the GW rises above the depth that provides sufficient overburden pressure for slickenside formation. As salts are introduced from saline to brackish water, clay soils may experience aggregate destabilization and destruction of soil structure as macropores are filled with clays, and soil crusts would likely form, reducing infiltration rates and increasing surface ponding after rain events. Soluble salts may concentrate at the soil surface as these ponds evaporate.

Salinization Due to Evaporative Demand

More distal, upland vertisols may experience enhanced desiccation as projected increases in ET and decreased precipitation are not offset by GW rise, or as elevated GW due to SLR is counteracted by anthropogenic withdrawals or reduced aquifer storage, as well as to elevated temperature and evaporative demands. Pronounced surface cracking due to soil dryness may enhance communication with the underlying brackish water table. Salinity in the GW is expected to generally increase due to evaporative demand, with pulses of freshwater additions from heavy precipitation events providing periodic rapid GW recharge, potentially resulting in localized freshening of GW as the bulk of the soil is bypassed due to rapid infiltration in the macropores (Kurtzman and Scanlon, 2011). In this scenario, salts concentrate in the soil matrix, increasing with depth and distance from desiccation cracks, as convective evaporation within cracks preferentially draws capillary water out of the soil body (Baram et al., 2013). In this scenario, vertic features are still likely to form, and soils may form more pedogenic carbonate, decreasing Ca^{2+} ions in solution relative to Na^+ and Mg^{2+}, resulting in increased sodicity (Srivastava et al., 2002). As salts are concentrated in the rooting zones, plants would experience increased ionic pressure and toxicity, resulting in ecosystem shifts in response to salinity rather than moisture status.

CONCLUSIONS

Pedogenic features and geochemical trends in mapped vertisols and vertic intergrades provide insight into the relative importance of salinization pathways within the Tatton Unit of ANWR. Underlying shallow brackish GW is a source of saliniza-

tion along proximal-distal transects in relatively upland environments and the floodplain of a tidal creek. The importance of non–GAS surface additions (storm surge, marine sediments, tidal influence) was greatest at sites proximal to St. Charles Bay. It decreased inland, although tidal creeks channels carried signatures of brackish surface additions farther inland.

Despite being mapped as vertisols and vertic intergrades, many sampled profiles lacked strongly developed vertic features. We propose that a combination of water availability and salinization interferes with the formation of desiccation cracks and slickensides characteristic of this soil order. We expect that hydrologic changes associated with climate change will act as controls on future pedogenesis at ANWR, with two potential end-members controlled by (1) increased saturation due to elevated GW associated with SLR at proximal or floodplain sites and (2) increased evaporation and communication with an increasingly saline deepening GW at distal/upland sites. Both pathways could contribute to the reduction of vertic properties by reducing pedoturbation associated with variable moisture content and by destroying soil aggregates by sodification, respectively. Similarly, both scenarios result in increased salinization at the soil surface as ponded brackish water evaporates and within the rooting zone from DCIS. Both scenarios promote ecosystem migration as changes in nutrient availability and osmotic potential will restrict halophobic vegetation.

This research has highlighted the need for continued, long-term observations of how soils, particularly vertic soils, respond to periodic to permanent inundation in natural systems.

ACKNOWLEDGMENTS

We want to recognize the Gulf Coast Association of Geological Societies and Baylor University's Department of Geosciences for financial support. Colt Sanspree and Andrew Stetter of ANWR provided permitting assistance and sampling site recommendations. Fieldwork could not have been completed without Bradley Kuehn. Steve Dworkin and Lyndsay DiPietro provided instruction and technical support for analytical instrumentation. Steve Dworkin, Lee Nordt, William Hockaday, and Joseph White served on Sarah Kogler's Ph.D. committee and suggested improvements to this manuscript. Finally, we want to recognize Rebecca Taormina's willingness to be a perpetual sounding board, particularly with figure development.

REFERENCES CITED

Abrol, I., J. Yadav, and F. Massoud, 1988, Salt-affected soils and their management: Food and Agriculture Organization of the United Nations (FAO) Soils Bulletin 39, 131 p.

Alizad, K., S. Hagen, S. Medeiros, M. Bilskie, J. Morris, L. Balthis, and C. Buckel, 2018, Dynamic responses and implications to coastal wetlands and the surrounding regions under sea level rise: PLoS ONE, v. 13, 27 p.

Baker, E., Jr., 1979, Stratigraphic and hydrogeologic framework of part of the coastal plain of Texas: Texas Department of Water Resources Report 236, 43 p.

Barnes, V., 1987, Geologic atlas of Texas Beeville–Bay City sheet: Bureau of Economic Geology, scale 1:250,000.

Baram, S., S. Ronen, D. Kurtzman, C. Kulls, and O. Dahan, 2013, Desiccation-crack-induced salinization in deep clay sediment: Hydrology and Earth System Sciences, v. 17, p. 1533–1545.

Barnard, P., and 10 additional authors, 2014, Dynamic flood modeling essential to assess the coastal impacts of climate change: Scientific Reports, v. 9, 13 p.

Blake, E., and D. Zelinsky, 2018, Hurricane Harvey: National Hurricane Center Tropical Cyclone Report, 77 p.

Blokhuis, W., 1982, Morphology and genesis of vertisols, *in* J. S. Kanwar, Chair, Vertisols and rice soils of the tropics: 12th International Congress of Soil Science, p. 23–48.

Butzler, R., and S. Davis, 2006, Growth patterns of Carolina wolfberry (*Lycium caroliniamum* L.) in the salt marshes of Aransas National Wildlife Refuge, Texas, USA: WETLANDS, v. 26, p. 845–853.

Callaway, J., R. DeLaune, and W. H. Patrick, Jr., 1997, Sediment accretion rates from four coastal wetlands along the Gulf of Mexico: Journal of Coastal Research, v. 13, p. 181–191.

Carroll, D., and H. Starkey, 1958, Effect of seawater on clay minerals: Clays and Clay Minerals, v. 7, p. 80–101.

Chowdhury, A., R. Boghici, and J. Hopkins, 2006, Hydrogeochemistry, salinity distribution, and trace constituents: Implications for salinity sources, geochemical evolution, and flow systems characterization, Gulf Coast Aquifer, Texas, *in* R. E. Mace, S. C. Davidson, E. S. Angle, and W. F. Mullican III, eds., Aquifers of the Gulf Coast of Texas: Texas Water Development Board Report 365, p. 81–128.

Chowdhury, A., B. Scanlon, R. Reedy, and S. Young, 2018, Fingerprinting groundwater salinity sources in the Gulf Coast Aquifer system, USA: Hydrogeology Journal, v. 26, p. 197–213.

Condon, L., A. Atchley, and R. Maxwell, 2020, Evapotranspiration depletes groundwater under warming over the contiguous United States: Nature Communications, v. 11, 8 p.

Coulombe, C., J. Dixon, and L. Wilding, 1996, Mineralogy and chemistry of vertisols: Developments in Soil Science, v. 24, p. 115–200.

Daliakopoulos, I., I. Tsanis, A. Koutroulis, N. Kourgialas, A. Varouchakis, G. Karatzas, and C. Ritsema, 2016, The threat of soil salinity: A European scale review: Science of the Total Environment, v. 573, p. 727–739.

Emanuel, K., 2017, Assessing the present and future probability of Hurricane Harvey's rainfall: PNAS, v. 114, p. 12681–12684.

Fall, A., 2017, Sustainable management of coastal saline soils in the Saloum river basin, Senegal: International Journal of Biological and Chemical Sciences, v. 11, p. 1903–1919.

FAO (Food and Agriculture Organization of the United Nations), 2021, Global map of salt-affected soils: FAO GSASmapv1.0: 20 p.

FEMA (Federal Emergency Management Agency), 2016, National Flood Insurance Program flood insurance rate maps, Aransas County, Texas: Maps 48007C0150G and 48007C0075G, scale 1:24,000.

Feng, X., C. Liu, F. Xie, J. Lu, L. Chiu, G. Tin-tera, and B. Chen, 2019, Precipitation characteristic changes due to global-warming in a high-resolution (16 km) ECMWF simulation: Quarterly Journal of the Royal Meteorological Society, v. 145, p. 303–317.

Fipps, G., 2021, Irrigation water quality standards and salinity management strategies: Texas A&M AgriLife Extension B–1667, 17 p.

Geilfus, C., 2019, Chloride in soil: from nutrient to soil pollutant: Environmental and Experimental Botany, v. 157, p. 299–309.

Hassani, A., A. Azapagic, and N. Shokri, 2021, Global predictions of primary soil salinization under changing climate in the 21st century: Nature Communications, v. 12, 17 p.

Hernandez, E., and V. Uddameri, 2014, Standardized precipitation evaporation index (SPEI)–based drought assessment in semi-arid South Texas: Environmental Earth Sciences, v. 71, p. 2491–2501.

Hoover, D., K. Odigie, P. Swarzenski, and P. Barnard, 2017, Sea-level rise and coastal groundwater inundation and shoaling at select sites in California, USA: Journal of Hydrology: Regional Studies, v. 11, p. 234–249.

Hoque, N., C. McNeil, and J. Granato, 2014, Projections of the population of Texas and counties in Texas by age, sex, and ethnicity from 2010–2050: University of Houston, Hobby Center for Public Policy, 217 p.

Hoegh-Guldberg, O., R. Cai, E. Poloczanska, P. Brewer, S. Sundby, K. Hilmi, V. Fabry, and S. Jung, 2014, The ocean, *in* V. R. Barros et al., eds., Fifth assessment report of the Intergovernmental Panel on climate change: Impacts, adaptation, and vulnerability, part B: Regional aspects: Cambridge University Press, p. 1655–1731.

Jones, A., J. McClelland, A. Hardison, and B. Hodges, 2019, Monitoring a riverine tidal freshwater zone (TFZ): HydroShare,

<https://www.hydroshare.org/resource/cb72a6f23d21459ab7fe9e72f55734b8/ >.

Jones, A., A. Hardison, B. Hodges, J. McClelland, and K. Moffett, 2020, Defining a riverine tidal freshwater zone and its spatiotemporal dynamics: Water Resources Research, v. 56, 17 p.

Junior, J., S. Furquim, A. Nascimento, R. Beirigo, L. Barbiero, V. Valles, E. Cuoto, and P. Vidal-Torrado, 2019, Salt-affected soils on elevated landforms of an alluvial megafan, northern Pantanal, Brazil: *Catena*, v. 172, p. 819–830.

Ketabchi, H., D. Mahmoodzadeh, B. Ataie-Ashtiani, and C. Simmons, 2016, Sea-level rise impacts on seawater intrusion in coastal aquifers: Review and integration: Journal of Hydrology, v. 535, p. 235–255.

Kishne, A., C. Morgan, and W. Miller, 2009, Vertisol crack extent associated with gilgai and soil moisture in the Texas Gulf Coast prairie: Soil Science Society of America Journal, v. 73, p. 1221–1230.

Kovda, I., 2020, Vertisols: Extreme features and extreme environment: *Geoderma* Regional, v. 22, 12 p.

Kloesel, K., and 14 other authors, 2018, Southern Great Plains, *in* D. R. Reidmiller, C. W. Avery, D. R. Easterling, K. E. Kunkel, K. L. M. Lewis, T. K. Maycock, and B. C. Stewart, eds., Impacts, risks, and adaptation in the United States: Fourth National Climate Assessment, Washington, D.C.: U.S. Global Change Research Program, v. 2, p. 987–1035.

Kurtzman, D., and B. Scanlon, 2011, Groundwater recharge through vertisols: Irrigated cropland vs. natural land, Israel: Vadose Zone Journal, v. 10, p. 662–674.

Kurtzman, D., S. Baram, and O. Dahan, 2016, Soil–aquifer phenomena affecting groundwater under vertisols: A review: Hydrology and Earth System Sciences, v. 20, p. 1–12.

Kutilek, M., 2001, Water relations and water management of vertisols: *in* Hydrologic processes in vertisols: Soil and Tillage Research, 33 p.

March, R., and E. Smith, 2012, Modeling potential coastal vegetation response to sea level rise and storm surge on estuarine peninsulas: Journal of Coastal Research, v. 28, p. 993–1007.

Mazhar, S., E. Pellegrini, M. Contin, C. Bravo, and M. Nobili, 2022, Impacts of salinization caused by sea level rise on the biological processes of coastal soils—A review: Frontiers in Environmental Science, v. 10, 18 p.

Mooney, R., and J. McClelland, 2012, Watershed export events and ecosystem responses in the Mission-Aransas National Estuarine Research Reserve, South Texas: Estuaries Coasts, v. 35, p. 1468–1485.

Moore, D. and R. Reynolds Jr., 1989, X–ray diffraction and the Identification and analysis of clay minerals. Oxford University Press, 332 p.

Mousavi, M., J. Irish, A. Frey, F. Olivera, and B. Edge, 2011, Global warming and hurricanes: The potential impact of hurricane intensification and sea level rise on coastal flooding: Climatic Change, v. 104, p. 575–597.

Nayak, K., A. Chinchmalatpure, R. Gururaja, and A. Verma, 2006, Shrink-swell potential of vertisols in relation to clay content and exchangeable sodium under different ionic environment: Journal of Indian Soil Science, v. 54, p. 1–5.

NOAA (National Oceanic and Atmospheric Administration), 2020, Relative sea level trend, 8774770, Rockport, Texas: Tides and currents sea level trends: Center for Operational Oceanographic Products and Services.

Nordt, L., L. Wilding, W. Lynn, and C. Crawford, 2004, Vertisol genesis in a humid climate of the coastal plain of Texas, U.S.A.: *Geoderma*, v. 122, p. 83–102.

NWS (National Weather Service), 2017, Major Hurricane Harvey—August 25–27, 2017: <https://www.weather.gov/crp/hurricane_harvey>.

Orlando, S., Jr., L. Rozas, G. Ward, and C. Klein, 1993, Salinity characteristics of Gulf of Mexico estuaries: National Oceanic and Atmospheric Administration (NOAA) Office of Ocean Resources Conservation and Assessment, 209 p.

Patarachao, B., D. Tyo, A. Zborowski, K. Davis, J. Kung, S. Ng, and P. Mercier, 2019, XRD analysis of illite-smectite in clays from oil sands ores: International Centre for Diffraction Data (ICDD), 11 p.

Pathak, A., and A. Fuller, 2021, Vulnerability and adaptation to climate change: An assessment for the Texas mid-coast: National Wildlife Federation Texas Coast and Water Program, 34 p.

Poppe, L., V. Paskevich, J. Hathaway, and D. Blackwood, 2001, A laboratory manual for x–ray powder diffraction: U.S. Geological Survey Open File Report 01–041, 89 p.

Porritt, G., 2021, Assessing drought trends within the Aransas National Wildlife Refuge: M.S. Thesis, University of Texas at San Antonio, 55 p.

Qadir, M., and S. Schubert, 2002, Degradation processes and nutrient constraints in sodic soils: Land Degradation and Development, v. 13, p. 275–294.

Qadir, M., S. Schubert, J. Oster, G. Sposito, P. Minhas, S. Cheraghi, G. Murtaza, A. Mirzabaev, and M. Saqib, 2018, High-magnesium waters and soils: emerging environmental and food security constraints: Science of the Total Environment, v. 642, p. 1108–1117.

Reich, M., T. Aghajanzadeh, J. Helm, S. Parmar, M. Hawkesford, and L. De Kok, 2017, Chloride and sulfate salinity differently affect biomass, mineral nutrient composition and expression of sulfate transport and assimilation genes in *Brassica rapa*: Plant and Soil, v. 411, p. 319–332.

Rengasamy, P., 2006, World salinization with an emphasis on Australia: Journal of Experimental Botany, v. 57, p. 1017–1023.

Richards, L. A., ed., 1954, Diagnosis and improvement of saline and alkali soils: U.S. Department of Agriculture Handbook 60, 166 p.

Rolston, D., J. Biggar, and D. Nielsen, 1984, Effect of salt on soils: California Agriculture, p. 11–13.

Rotzoll, K., and C. Fletcher, 2012, Assessment of groundwater inundation as a consequence of sea-level rise: Nature Climate Change, v. 3, p. 477–481.

Royer, D., 1999, Depth to pedogenic carbonate horizon as a paleoprecipitation indicator: Geology, v. 27, p. 1123–1126.

Runkle, J., K. Kunkel, J. Nielsen-Gammon, R. Frankson, S. Champion, B. Stewart, L. Romolo, and W. Sweet, 2017, Texas State Climate Summary: National Oceanic and Atmospheric Administration Technical Report NESDIS 149–TX, 4 p.

Sawyer, A., H. Michael, and A. Schroth, 2016, From soil to sea: the role of groundwater in coastal critical zone processes: WIREs Water, v. 3, p. 706–726.

Schofield, R., and M. Kirkby, 2003, Application of salinization indicators and initial development of global soil salinization scenario under climatic change: Global Biogeochemical Cycles, v. 17, p. 1078–1091.

Shafer, G., 1970, Groundwater resources of Aransas County, Texas: Texas Water Development Board Report 124, 70 p.

Shahid, S., and D. Jenkins, 1992, Micromorphology of surface and subsurface sealing and crusting in the soils of Pakistan, *in* W. F. Vlotman, eds., Subsurface drainage on problematic irrigated soils: Sustainability and cost effectiveness. Proceedings of the 5th International Drainage Workshop, v. 2, p. 177–189.

Shahid, S., M. Zaman, and L. Heng, 2018, Introduction to soil salinity, sodicity, and diagnostic techniques, *in* Guideline for salinity assessment, mitigation, and adaptation using nuclear and related techniques: Springer, 42 p.

Srivastava, P., T. Bhattacharyya, and D. Kumar Pal, 2002, Significance of the formation of calcium carbonate minerals in the pedogenesis and management of cracking clay soils (vertisols) of India: Clays and Clay Minerals, v. 50, p. 111–126.

SSS (Soil Survey Staff), 1996, Soil survey laboratory method manuals: U.S. Department of Agriculture Natural Resources Conservation Service Soil Survey Investigation Report 4, v. 3, 700 p.

SSS (Soil Survey Staff), 1999, Soil taxonomy, 2nd ed.: U.S. Department of Agriculture Handbook 436, 886 p.

SSS (Soil Survey Staff), 2023, Web soil survey: U.S. Department of Agriculture Natural Resources Conservation Service, <http://websoilsurvey.sc.egov.usda.gov/>.

Sui, H., D. Chen, J. Yan, B. Li, W. Li, and B. Cui, 2022, Soil salinity estimation over coastal wetlands based on random forest algo-

rithm and hydrological connectivity metric: Frontiers in Marine Science, v. 9, 15 p.

Svensson, T., H. Kylin, M. Montelius, P. Sanden, and D. Bastviken, 2021, Chlorine cycling and the fate of Cl in terrestrial environments: Environmental Science and Pollution Research International, v. 28, p. 7691–7709.

Swarzenski, P., H. Dulai, K. Kroeger, C. Smith, N. Dimova, C. Storlazzi, N. Prouty, S. Gingerich, and C. Glenn, 2017, Observations of nearshore groundwater discharge: Kahekili Beach Park submarine springs, Maui, Hawaii: Journal of Hydrology: Regional Studies, v. 11, p. 147–165.

Taalab, A., G. Ageeb, H. Siam, and S. Mahmoud, 2019, Some characteristics of calcareous soils: A review: Middle East Journal of Agriculture Research, v. 8, p. 96–105.

Tremblay, T., J. Vincent, and T. Calnan, 2008, Status and trends of inland wetland and aquatic habitats in the Corpus Christi area: Final Report prepared by the Bureau of Economic Geology for the Coastal Bend Bays and Estuaries Program, Texas General Land Office, and National Oceanic and Atmospheric Administration under CBBEP Contract 0722 , 101 p.

Tully, K., and 10 additional authors, 2019a, The invisible flood: the chemistry, ecology, and social implications of coastal saltwater intrusion: BioScience, v. 69, p. 368–378.

Tully, K., D. Weissman, W. Wyner, J. Miller, and T. Jordan, 2019b, Soils in transition: saltwater intrusion alters soil chemistry in agricultural fields: Biogeochemistry, v. 142, p. 339–356.

TWDB (Texas Water Development Board), 2023, Water data interactive, groundwater data viewer: Aransas County: <https://www3.twdb.texas.gov/apps/WaterDataInteractive/GroundWaterDataViewer>.

Uddameri, V., V. Honnungar, and E. Hernandez, 2014, Assessment of groundwater water quality in central and southern Gulf Coast aquifer, TX using principal component analysis: Environmental Earth Science, v. 71, p. 2653–2671.

USACoE (U.S. Army Corps of Engineers), 1995, Gulf Intracoastal Waterway–Aransas National Wildlife Refuge, Texas: Feasibility report and final environmental impact statement: Volume 1, main report: 279 p.

USFWS, (U.S. Fish and Wildlife Service), 2010, Aransas National Wildlife Refuge complex: Comprehensive conservation plan and environmental assessment, 369 p.

UT–MS (University of Texas Marine Science InstituteU, 2015, Mission-Aransas National Estuarine Research Reserve Management Plan 2015–2020 for the National Oceanic and Atmospheric Administration Office of Coastal Management, 267 p.

Veron, F., 2015, Ocean spray: Annual Review of Fluid Mechanics, v. 47, p. 507–538.

Virmani, S., K. Sahrawat, and J. Burford, 1982, Physical and chemical properties of vertisols and their management, *in* J. S. Kanwar, Chair, Vertisols and rice soils of the tropics: 12th International Congress of Soil Science, p. 80–93.

Walker, J., R. Kopp, C. Little, and B. Horton, 2022, Timing of emergence of modern rates of seal-level rise by 1863: Nature Communications, v. 13, 8 p.

Watanabe, M., 2015, Sample preparation for x–ray fluorescence analysis IV. Fusion bead method—Part 1, basic principles: Rigaku Journal, v. 31, 6 p.

Wicke, B., E. Smeets, V. Dornburg, B. Vashev, T. Gaiser, W. Turkenburg, and A, Faaij, 2011, The global technical and economic potential of bioenergy from salt-affected soils: Energy and Environmental Science, v. 4, p. 2669–2681.

West, A., and M. Wetz, 2021, Water quality status and trends in bays of the Texas Coastal Bend: Coastal Bend Bays and Estuaries Program Publication 149, 77 p.

White, P., and M. Broadley, 2003, Calcium in plants: Annals of Botany, v. 94, p. 487–511.

Weissman, D., and K. Tully, 2020, Saltwater intrusion affects nutrient concentrations in soil porewater and surface waters of coastal habitats: Agroecosystems, v. 11, p. 1–19.

Wong, V., S. Johnston, E. Burton, P. Hirst, L. Sullivan, R. Bush, and M. Blackford, 2015, Seawater inundation of coastal floodplain sediments: Short-term changes in surface water and sediment geochemistry: Chemical Geology, v. 398, p. 32–45.

Xiao, H., D. Wang, S. Medeiros, M. Bilskie, S. Hagen, and C. Hall, 2019, Exploration of the effects of storm surge on the extent of saltwater intrusion into the surficial aquifer in coastal east-central Florida (USA): Science of the Total Environment, v. 648, p. 1002–1017.

Xie, W., J. Yang, S. Gao, R. Yao, and X. Wang, 2022, The effect and influence mechanism of soil salinity on phosphorus availability in coastal salt-affected soils: Water, v. 14, 15 p.

Yan, N., P. Marschner, W. Cao, C. Zuo, and W. Quin, 2015, Influence of salinity and water content on soil microorganisms: International Soil and Water Conservation Research, v. 3, p. 316–323.

Yao, Q., K. Liu, H. Williams, S. Joshi, T. Bianchette, J. Ryu, and M. Dietz, 2019, Hurricane Harvey storm sedimentation in the San Bernard National Wildlife Refuge, Texas: Fluvial versus storm surge deposition: Estuaries and Coasts, v. 43, 13 p.

Young, S., P. Knox, E. Baker, S. Hamlin, B. Galloway, and N. Deeds, 2010, Hydrostratigraphy of the Gulf Coast Aquifer from the Brazos River to the Rio Grande: Texas Water Development Board Report, 213 p.

Zhang, T., and S. Wang, 2019, Explanation of the influence of sodium chloride solution on volume deformation and permeability of normally consolidated clays: Materials (Basel), v. 12, 10 p.

APPENDIX

Table A–1. Soil field descriptions.

Site	Horizon	Depth (cm)	Textural Class	Color	Redox. Features	Carbonates	Other
1–1	A	4	CfS	7.5YR 5/2	Fine ox. root	-	Granular structure, absent-weak
	Bw	16	S	7.5YR 5/1	Few, fine ox. roots	-	-
	2Btk	50	SC	2.5Y 4/2	Few, faint ox. masses	Common, fine diffuse masses	Fine linear charcoal
	2Btk2	65	SC	10YR 5/2	Common, fine 10YR 6/3	Few, fine nodules	Saline-brackish GW
1–2	A	6	CL	5Y 3/1	Common, fine ox. roots	Few, fine nodules	Fine charcoal
	Bwg	30	CL	Intercalated 5YR 5/1 and 5YR 6/1	Common, fine ox. roots	Common, fine nodules, increasing with depth	-
	Btk	53	LC	7.5YR 5/1	Few, fine ox. root traces	Common, coarse nodules	-
	Btkyg	70	SC	5YR 5/1	-	Common, coarse nodules	Gypsum; weak SBK structure; saline-brackish GW
1–3	A	3	SL	10YR 3/1	-	-	Weak granular structure, few root, charcoal present
	Bw	15	fS	10YR 5/2	-	-	Few roots
	2Bt	40	SC/C	10YR 4/2 to 7.5YR 6/1	-	Fine powdery masses	Weak ABK structure
	2Btk	70	SC	7.5YR 6/2	-	Coarse powdery masses, few fine nodules	Few, fine dark masses
	2Btkg	80	C	2.5Y 6/1	-	Common, fine nodules	-
	2Btg	95	C	2.5Y 5/1	-	-	2.5Y 5/3 fine sand lenses in macropores
1–4	A	9	CL	2.5Y 2.5/1	-	-	Many penetrating roots; partially degraded wood fragments; wetting front 10cm
	Btg1	42	LC	2.5Y 3/1	-	-	ABK peds, clay alignment on pressure faces
	Btkg1	56	SC	10YR 4/1	-	Coarse nodule strings in dissolution cavities	-
	Btkg2	80	LC	2.5Y 4/1	-	Many, fine nodules, increasing in size with depth	-
	Btg2	95	C	2.5Y 6/1	-	-	-
1–5	Ap	10	CL	7.5YR 2.5/1	Very fine, 7.5YR 3/3	-	Granular structure, many roots
	Bwg	18	SC	7.5YR 3/1	Few, ox. root traces	-	Few pressure fissures, sand pockets in macropores
	Bssg	40	C	10YR 3/1	-	Few, fine nodules	Fissile-firm ABK structure, weak vertic shear planes
	Bkssg1	80	C	10YR 4/1	-	Common, fine nodules, increasing with depth	Common slickensides, clay films on ped boundaries
	Bkssg2	105	SiC	10YR 5/1		Few, coarse nodules	Very plastic

2–1	A	1	L	2.5Y 7/1	-	-	Minimal soil development, overwash sand
	Btkg	19	CL	2.5Y 4/1	-	Common, fine nodules	2.5Y 7/1 sand-filled burrows; many roots; firm ABK to SBK
	Btkg2	46	SC	2.5Y 4/1	Coarse conc.	Freq., fine nodules	2.5Y 7/2 sand-infilled burrows; firm SBK structure; 15% coarse fragments*
	Btg	67	SCL	G1 5/1	Few, 5YR 5/6	Common, coarse nodules	Sand lenses, G1 6/1; 11% coarse fragments*; GW EC: 71.9mS/cn
	Btg2	75	C	G1 4/1	Few, white-light greenish grey	Freq., fine nodules	-
	2Oa	82	Muck	G1 2.5-1 to 2.5N	-	-	H_2S odor
2-2	A	2	CL	5Y 5/2 S 5Y 3/1 OM	-	In burrow linings	Interlaminated microbial texture, many fine roots, coarse burrows
	Btg	19	CL	5Y 3/1	-	Fine nodules	Strong ABK structure; 0.1% gypsum*
	Btkg	25	CL	G4/1	Weak, fine G8/1	Few coarse unconsolidated masses, many fine nodules	Highly bioturbated; 0.1% gypsum*
	Btk	35	C	2.5Y 6/2	-	Sharp, jagged fine aggregates	Highly bioturbated, 0.1% gypsum*
	Btk2	65	C	2.5Y 7/4	Fine, freq. 7.5YR 7/6	Many, fine nodules	Y–shaped reduced and unconsolidated burrow, shell fragments; 6.8% gypsum*; GW EC: 89.2 mS/cm
2-3	A	19	VFSL	10YR 4/1 C 10YR 6/2 SC	-	-	Interbedded C and SC, weak granular structure
	Bw	30	C	10YR 4/2	-	-	Contrasting material in soil cracks; 10% coarse fragments*
	Btkg	71	C	2.5Y 4/1	5YR 4/3 on fine root traces	Fine masses at top, fine nodules at base	Highly bioturbated, 5 mm burrow openings, SBK to wedge structure; 6% coarse fragments*; GW EC: 48mS/cm
	Btk	90	C	2.5YR 7/2	-	Few, fine nodules	10% coarse fragments*
	Btk2 (2BC)	105	C		-	Fine nodules	Very sticky; 5% coarse fragments*
2-4	A	15	SCL	2.5Y 3/1	-	-	Many roots, horizontal burrows, burrow shafts infilled with S
	Bw	27	SCL	2.5YR 4/2	-	--	Coarse open burrows, fine roots
	Bw2	49	SCL	2.5Y 7/2	-	-	Clay infilled burrows
	Btk	80	SCL	2.5Y 6/2	Fine, 7.5Y 5/6	Common, fine nodules	Highly bioturbated, fewer macroscopic burrows, GW EC: 80 mS/cm
	Bt	95	C		-	-	Very sticky

S., sand; LS, loamy sand; SCL, sandy clay loam; L, loam; SiL, silt loam; SiCL, silty clay loam; C, clay; CL, clay loam; SC, sandy clay; SiC, silty clay; OM, organic matter; ABK, angular blocky structure; and SBK, subangular blocky structure.

Asterisks indicate source from lab analysis done by the Texas A&M Soil Testing Laboratory rather than field observations.